

Learning Dynamical Systems Encoding Non-Linearity within Space Curvature

Journal Title
XX(X):1-19
©The Author(s) 2024
Reprints and permission:
sagepub.co.uk/journalsPermissions.nav
DOI: 10.1177/ToBeAssigned
www.sagepub.com/

SAGE

Bernardo Fichera¹ and Aude Billard¹

Abstract

Dynamical Systems (DS) are an effective and powerful means of shaping high-level policies for robotics control. They provide robust and reactive control while ensuring the stability of the driving vector field. The increasing complexity of real-world scenarios necessitates DS with a higher degree of non-linearity, along with the ability to adapt to potential changes in environmental conditions, such as obstacles. Current learning strategies for DSs often involve a trade-off, sacrificing either stability guarantees or offline computational efficiency in order to enhance the capabilities of the learned DS. Online local adaptation to environmental changes is either not taken into consideration or treated as a separate problem. In this paper, our objective is to introduce a method that enhances the complexity of the learned DS without compromising efficiency during training or stability guarantees. Furthermore, we aim to provide a unified approach for seamlessly integrating the initially learned DS's non-linearity with any local non-linearities that may arise due to changes in the environment. We propose a geometrical approach to learn asymptotically stable non-linear DS for robotics control. Each DS is modeled as a harmonic damped oscillator on a latent manifold. By learning the manifold's Euclidean embedded representation, our approach encodes the non-linearity of the DS within the curvature of the space. Having an explicit embedded representation of the manifold allows us to showcase obstacle avoidance by directly inducing local deformations of the space. We demonstrate the effectiveness of our methodology through two scenarios: first, the 2D learning of synthetic vector fields, and second, the learning of 3D robotic end-effector motions in real-world settings.

Keywords

dynamical system, learning from demonstration, control, differential geometry, manifold

1 Introduction

Learning from Demonstration (LfD) represents a powerful approach to derive global behavioral policies for high-level closed-loop control by observing demonstrated tasks. Such policies are represented using the mathematical framework of Dynamical Systems (DS), namely a vector field $\mathbf{f} : \mathbb{R}^d \rightarrow \mathbb{R}^d$, mapping the d -dimensional input state $\mathbf{x}(t) \in \mathbb{R}^d$ to its time-derivative $\dot{\mathbf{x}}(t) \in \mathbb{R}^d$, such that $\dot{\mathbf{x}}(t) = \mathbf{f}(\mathbf{x})$.

In the field of robotics, this framework is commonly employed for describing and regulating various motion types, such as point-to-point motions characterized by fixed-point stable equilibrium DS, or periodic motions featuring stable limit-cycle DS. The stability of a learned DS becomes a significant concern when it is applied in closed-loop control systems. Using standard regression methods to learn the mapping \mathbf{f} provides no inherent guarantee of producing stable control policies. A wealth of learning approaches have been developed in the last decades to learn a DS with the stability guaranteed. They follow two fundamental paths: 1) constraint optimization; 2) learning of complex potential function via diffeomorphism.

In the first category, the most popular approach is to derive constraints via Lyapunov's second method for stability. In the beginning, [Khansari-Zadeh and Billard \(2011\)](#) utilized a quadratic Lyapunov function to establish stability conditions in a Gaussian Mixture Regression (GMR) problem for learning Dynamical Systems (DS). However, stability

guarantee imposes a severe restriction on the learnable complexity of the DS and prevents learning highly non-linear DS containing high-curvature regions or non-monotonic motions (i.e., temporally moving away from the attractor). More recent approaches tried to alleviate this issue by improving the complexity of the Lyapunov function adopted as constraint, [Figueroa and Billard \(2018\)](#). Specifically, by moving towards an elliptic Lyapunov function, these approaches are capable of relaxing the constraints allowing for learning more complicated trajectories. Nevertheless, they still struggle in learning DS exhibiting high non-linearity and non-monotonic behavior in different radial directions with respect to the equilibrium point.

An alternative constraint optimization problem can be derived from Contraction Theory (CT), [Lohmiller and Slotine \(1998\)](#). Abstracting from the absolute position of the equilibrium point, CT follows a differential perspective. Conditions derived by CT impose local contraction of trajectories implying, as a consequence, global exponential stability towards the equilibrium point. [Blocher et al. \(2017\)](#) takes advantage of CT to derive a stabilizing controller that

¹École Polytechnique Fédérale de Lausanne, Lausanne, Switzerland

Corresponding author:

Bernardo Fichera, Learning Algorithms and Systems Laboratory, École Polytechnique Fédérale de Lausanne, Lausanne, Switzerland.

Email: bernardo.fichera@epfl.ch

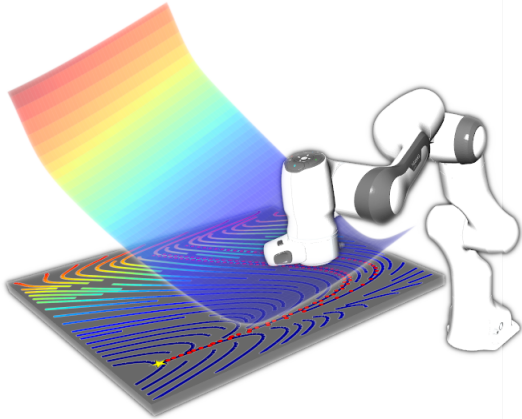


Figure 1. End-effector motion of a robotic arm guided by a 2D learned DS. The surface corresponds to the 3D Euclidean space embedded representation of the learnt 2D manifold. The color gradient represents the value of the potential function that drives the linear vector field taking place on the 2D manifold. The manifold's curvature induces "apparent" non-linearity in the 2D chart Euclidean space representation of the vector field taking place on the 2D manifold. During the learning process, the curvature of the manifold adapts so that the streamlines of the 2D chart Euclidean space representation of the vector field follow closely the demonstrated trajectories (red dots), preserving the stability towards a desired equilibrium point (yellow star).

eliminates potential spurious attractor present in the DS learned without stability constraints. [Sindhvani et al. \(2018\)](#) uses CT to derive constraints for learning DS in a Support Vector Regression problem. Both [Blocher et al. \(2017\)](#) and [Sindhvani et al. \(2018\)](#) rely on non-generalized contraction analysis, which, in turn, results in overly conservative constraints. This is analogous to the adoption of a simplistic quadratic function in the Lyapunov approach to the stability problem. In their work, [Ravichandar et al. \(2017\)](#) introduced a GMR-based regression problem, incorporating stability constraints derived from generalized (CT) analysis. While this approach demonstrates superior performance by relaxing overly conservative constraints, it does so at the expense of achieving global stability, focusing solely on local stability.

Another approach to learning DS involves the existence of a *latent* space, in which either the Lyapunov function is quadratic or the DS is linear. In these approaches, the focus is on learning a diffeomorphism $\psi : \mathbb{R}^d \rightarrow \mathbb{R}^d$ between the original space and the latent one. A first example of this approach for solving the stability vs accuracy dilemma was proposed by [Neumann and Steil \(2015\)](#). This approach extends the applicability of SEDS by introducing a diffeomorphic mapping that transforms non-quadratic Lyapunov functions, ensuring point-wise stability of the demonstrated trajectory, into quadratic forms. After applying SEDS in this transformed space, the desired policy is obtained through the application of the inverse diffeomorphic mapping. More recent approaches concentrate on directly identifying latent spaces where the DS exhibits linear behavior. These methods make use of an approximation of the Large Deformation Diffeomorphic Metric Mapping (LDDMM) framework, [Joshi and Miller](#)

(2000), to accommodate the required smoothness constraints in the mapping.

In [Perrin and Schlehuber-Caissier \(2016\)](#), the diffeomorphic learning DS is fundamentally geometric, focusing solely on the positions of the original and target points. To reconstruct the proper velocity profile, a rescaling of the learned DS is employed. The diffeomorphic map is learned as sequence locally weighted translations applied to the points in the original space. Additionally, more modern and network-based strategies, such as non-volume preserving transformation (NVP) [Dinh et al. \(2016\)](#), can be utilized to model the diffeomorphic map. [Rana et al. \(2020\)](#) adopts NVP transformations within an optimization framework that incorporates dynamic information, specifically velocity, into the process. This results in a one-step learning algorithm. Essentially, all these approaches involve learning a complex potential function whose gradient closely follows the target DS. While these methods demonstrate improved performance, they come with the trade-off of requiring sophisticated machinery for creating a function approximator capable of learning a mapping that exhibits the diffeomorphic property mandated by the proposed mathematical framework.

All the methods discussed above are confined to learning first-order conservative DS. Dissipative or second-order DS cannot be learned within this framework. Moreover, online local adaptation to environmental changes is not considered as part of the problem. In DS-based control, such issues are typically addressed a-posteriori and handled through a modulation matrix, as in [Khansari-Zadeh and Billard \(2012\)](#). These approaches are agnostic to the DS they aim to modulate, potentially leading to spurious attractors whenever the DS velocity direction aligns with the normal principal direction of the modulation matrix. A clever trick to partially address this problem involves breaking orthogonality between the modulation matrix's principal components, as proposed by [Huber et al. \(2019\)](#). However, these methods rely on manually designing modulation matrices for each local adaptation they aim to accommodate, resulting in increased complexity in both problem design and stability analysis. The application of modulation to second-order systems remains unclear.

These limitations cast a shadow over DS methods when compared to planning methods. Planning methods, armed with inherent adaptability and increasingly efficient sampling-based strategies, [Williams et al. \(2017\)](#), are gradually overcoming their reactivity challenges, fueled by advancements in computational hardware power, as shown in [Bhardwaj et al. \(2021\)](#). In response to this, geometry-based DS shaping approaches, drawing on tools from the field of differential geometry, emerge as a solution to reverse this trend. These approaches aim to achieve two crucial objectives: 1) enhance DS policies with greater expressivity and bolster their adaptability, and 2) broaden the modularity of the approach to tackle the growing complexity of real-world scenarios in which robotic systems must operate.

Drawing inspiration from [Bullo and Lewis \(2005\)](#), [Ratliff et al. \(2018\)](#) introduced the Riemannian Motion Policy (RMP), a modular mathematical framework for robotic motion generation. In contrast to prior works, this approach produces second-order DS, the specific behavior of which is inherently linked to a Riemannian metric. By carefully

designing such metrics, a wide range of behaviors can be exhibited and combined.

With few exceptions, detailed in Section 2, this research line has not explicitly focused on Learning from Demonstration (LfD). Instead, the emphasis has been on expanding the capabilities of the mathematical framework to enhance the complexity and variety of reproducible behaviors. Building upon RMP, Cheng et al. (2020) proposed RMPflow, which effectively combines different tasks designed via RMPs, leveraging the sparsity of the structure for computational efficiency.

Summarizing the endeavors of previous works, Bylard et al. (2021) provides a principled and geometrically consistent description of the mathematical framework used for geometry-based policies. Current research in the field is shifting towards a more general formalism, extending beyond Riemannian differentiable manifolds to include Finsler structures, as discussed in Xie et al. (2021); Ratliff et al. (2021). This expansion aims to introduce velocities as a fundamental ingredient in shaping metrics that define policies' behavior.

Contribution

Our work bridges the gap between DS learning literature and the evolving field of geometry-based shaping of DS policies. From the DS learning literature, we draw inspiration from concepts related to the existence of a latent space. A notable distinction is that we do not enforce diffeomorphic constraints. On the other hand, we borrow from the Geometric DS literature the idea of a chart-based representation of DS occurring on a manifold, along with employing various tools from differential geometry to define the operators we utilize.

In this work, we introduce a novel approach to learning DS that aims to integrate LfD with modern geometric control techniques. Within our framework, the non-linearity of the DS is "encoded" within the curvature of a $d + 1$ -dimensional latent manifold, where d represents the dimension of the vector field being learned. This concept is illustrated in Figure 1.

Our framework naturally extends to second-order dissipative DS and easily adapts to potential online local non-linearity changes, such as those arising from the presence of obstacles. Additionally, we propose a variety of solutions, such as directional and exponential, to make the usage second-order DS effective in LfD scenario. The proposed geometric framework, as indicated by standard metrics for evaluating learning performance, matches or outperforms the state-of-the-art while achieving notably lower computational costs during both training and query phases. These efficiency gains are obtained without compromising the performance or stability of the learned DS. Furthermore, such framework amplifies the expressivity of geometrical policies, shedding light on the relationship between DS non-linearity and manifold curvature. It also provides an explicit visualization of the Euclidean embedded representation of the latent manifold responsible for generating non-linearity.

To operationalize this work, we developed a fully differentiable PyTorch library*, which can be used for both Learning from Demonstration (LfD) and manually shaping geometric policies. In second-order settings, such

policies can exhibit either geodesic or damped harmonic behavior, expanding the variety of behaviors available. To preserve reactive control features, we developed a high-performance C++ library†, that integrates our geometrical DS with fast one-step model-based or model-free Quadratic Programming control techniques. Additionally, the fully-templated nature of the library allows for the generalization of the controllers' suite to different non-Euclidean spaces, such as Lie Groups. In practical terms, for robot end-effector control, this represents a valuable feature for $\mathbb{R}^3 \times \text{SO}(3)$ control, where one controller operates in the three-dimensional Euclidean space, while the other one functions in the Special Orthogonal Group characterizing orientation space. The control strategy is fully modular and easily integrable in RMP frameworks as in Fichera and Billard (2023).

2 Related work

Our method differs from Rana et al. (2020) by avoiding the need to learn a diffeomorphism between two chart representations of a manifold. Instead, we focus on learning an embedding for a higher-dimensional Euclidean representation, which is computationally efficient and offers more expressive models. Our approach is less mathematically restrictive, requiring only a homeomorphic relationship between the manifold and its embedding, and can use any continuous function approximator, bypassing the need for specific Non-Volume Preserving (NVP) networks. This leads to a simpler and quicker optimization process. Additionally, our method allows to construct second-order DSs, while still accommodating first-order DSs. This flexibility enhances our model's ability to handle complex tasks, such as replicating crossing trajectories and navigating around concave obstacles using a combination of geodesic and harmonic motions.

While not directly classified as part of the LfD literature, Mukadam et al. (2019) applies learning methods in RMPflow by introducing weight functions that hierarchically modify the Lyapunov functions associated with subtasks. This enhancement improves the overall performance of the combined policy. Contrastingly, our approach primarily focuses on learning the curvature of the manifold. This enables the generation of complex policies without incurring in stability problems caused by the lack of convexity of the Lyapunov function.

In the work presented in Rana et al. (2019), the emphasis lies in learning the Cholesky decomposition of the metric tensor. When compared with our approach, this method not only exhibits limitations by solely addressing first-order geometry but also mandates specifically designed and more complex function approximators to learn the lower diagonal matrix of the metric tensor Cholesky decomposition. This structure limits the flexibility to dynamically adjust the local geometry of the space to handle scenarios, such as obstacle avoidance.

*learn-embedding code available at:

<https://github.com/nash169/learn-embedding>

†control-lib code available at:

<https://github.com/nash169/control-lib>

Beik-Mohammadi et al. (2021) developed a method to generate geodesic motions aligned with observed trajectories by deriving a Riemannian metric from a map between the original and a latent space, learned through a Deep Autoencoder. This involves geodesic motions generated via an iterative optimization process that minimizes the curve length between two points. Conversely, our method focuses on constructing a DS formulation, ensuring stability, reactivity, and robustness against spatial and temporal disturbances typical in DS-based control. We directly access the manifold as a higher-dimensional Euclidean representation by approximating a single embedding component through a simple feedforward network, eliminating the need for complex Deep Learning structures. This not only enhances computational efficiency but also provides much greater expressivity, allowing a deeper understanding of why and how altering manifold's curvature to achieve the desired DS non-linearity. Our framework allows for a directly modifiable embedding designed to facilitate online local deformation.

3 Background

The presentation of the work relies heavily on concepts from differential geometry. Our notation follows do Carmo (1992). We employ the Einstein summation convention in which repeated indices are implicitly summed over.

Given a set, \mathcal{M} , and a Hausdorff and second-countable topology, \mathcal{O} , a topological space $(\mathcal{M}, \mathcal{O})$ is called a d -dimensional manifold if $\forall p \in \mathcal{M} : \exists \mathcal{U} \in \mathcal{O} : \exists x : \mathcal{U} \rightarrow x(\mathcal{U}) \subseteq \mathbb{R}^d$, with x and x^{-1} continuous maps. (\mathcal{U}, x) is a *chart* of the manifold $(\mathcal{M}, \mathcal{O})$. x is called the *chart map*; it maps $p \in \mathcal{M}$ to the point $x(p) = (x^1(p), \dots, x^d(p))$ into the \mathbb{R}^d Euclidean space. $(x^1(p), \dots, x^d(p))$ are known as the coordinate maps or local coordinates. With slight abuse of notation, we will refer to a point in \mathbb{R}^d using the bold vector notation $\mathbf{x} = x(p)$, dropping the explicit dependence on $p \in \mathcal{M}$. x^i will be i -th local coordinate of $\mathbf{x} \in \mathbb{R}^d$.

Throughout, we will denote with \mathcal{M} a *differentiable Riemannian* manifold, that is a manifold endowed with a C^∞ -atlas, \mathcal{A} , and a $(0, 2)$ -tensor field, g , with positive *signature*, satisfying symmetry and non-degeneracy properties. We refer to g as a *Riemannian metric*.

$T_p\mathcal{M}$ ($T_p^*\mathcal{M}$) denotes the tangent (resp. cotangent) space at $p \in \mathcal{M}$. We denote by $v_p \in T_p\mathcal{M}$ a vector in the tangent space at p . Given a set of local coordinates (x^1, \dots, x^d) , in a neighborhood \mathcal{U} of $p \in \mathcal{M}$, we denote by $\frac{\partial}{\partial x^i}$ (resp. dx^i) the i -th basis vector of $T_p\mathcal{M}$ (resp. $T_p^*\mathcal{M}$). The tangent bundle $T\mathcal{M}$ (resp. cotangent bundle $T^*\mathcal{M}$) is the disjoint union of these tangent (resp. cotangent) spaces over all $p \in \mathcal{M}$.

A vector field (resp. covector field) X on $\mathcal{U} \subset \mathcal{M}$ is a map assigning to each point $p \in \mathcal{U}$ a vector $X(p) \in T_p\mathcal{M}$ (resp. $X(p) \in T_p^*\mathcal{M}$). $\Gamma(T\mathcal{M})$ (resp. $\Gamma(T^*\mathcal{M})$) denotes the set of vector (resp. covector) fields on \mathcal{M} . Let $X, Y \in \Gamma(T\mathcal{M})$, the vector field $\nabla_Y X$ is the covariant derivative of X with respect to Y . In the context of dynamical systems subjected to external driving forces on manifolds, a force at a point $p \in \mathcal{M}$ is a covector, namely $f_d : T_p\mathcal{M} \times I \rightarrow T_p^*\mathcal{M}$.

The metric can be used to uniquely relate elements of $T\mathcal{M}$ and elements of $T^*\mathcal{M}$. For each $p \in \mathcal{M}$ we define the

flat map $(\cdot)^\flat : T_p\mathcal{M} \rightarrow T_p^*\mathcal{M}$ and sharp map $(\cdot)^\sharp : T_p^*\mathcal{M} \rightarrow T_p\mathcal{M}$ as the inverse of $(\cdot)^\flat$.

$C^\infty(\mathcal{M})$ denotes the set of smooth functions $\varphi : \mathcal{M} \rightarrow \mathbb{R}$. The differential of a function $\varphi \in C^\infty(\mathcal{M})$ is the covector field $d\varphi \in \Gamma(T^*\mathcal{M})$. In local coordinates, $d\varphi = \frac{\partial \varphi}{\partial x^i} dx^i$. To express the partial derivative, we will adopt the contracted notation $\partial_i \varphi = \frac{\partial \varphi}{\partial x^i}$.

Let \mathcal{M} and \mathcal{N} be two differentiable Riemannian manifolds and $f : \mathcal{M} \rightarrow \mathcal{N}$ be a continuous map. The *pushforward* map f_* is the map $f_* : T\mathcal{M} \rightarrow T\mathcal{N}$ where $f_*(X)\varphi := X(f \circ \varphi) \quad \forall \varphi \in C^\infty(\mathcal{N}), \forall X \in \Gamma(T\mathcal{M})$. The *pullback* map f^* is the map $f^* : T^*\mathcal{N} \rightarrow T^*\mathcal{M}$, where $f^*(\omega)(X) := \omega(f_*(X)) \quad \forall X \in \Gamma(T\mathcal{M}), \forall \omega \in T^*\mathcal{N}$.

A curve γ on a given manifold \mathcal{M} is a mapping $\gamma : I \subset \mathbb{R} \rightarrow \mathcal{M}$. The curve can be expressed in local coordinate through the mapping $x_\gamma = x \circ \gamma : I \rightarrow \mathbb{R}^d$ such that $x(\gamma(t)) = x_\gamma(t) \in \mathbb{R}^d$ for each $t \in I$. We use $\dot{x}_\gamma(t)$ to express the *speed* $\frac{dx_\gamma}{dt}$. Wherever the explicit reference to the underlying curve is not needed, we use directly \dot{x}^i to indicate the i -th local coordinate of the velocity of the curve.

Given a curve $\gamma : I \rightarrow \mathcal{M}$, a vector field along γ , v_γ , is a map that assigns to each $t \in I$ an element $v_{\gamma(t)} \in T_{\gamma(t)}\mathcal{M}$. The covariant derivative of v_γ along v_γ in local coordinates is

$$(\nabla_{v_\gamma} v_\gamma)^k = \ddot{x}^k + \Gamma_{ij}^k \dot{x}^i \dot{x}^j, \quad (1)$$

with Γ_{ij}^k the Christoffel symbols. A Riemannian metric g induces a unique affine connection ∇ on \mathcal{M} , called the Levi-Civita connection. In this scenario the Christoffel symbols can be expressed as a function of the Riemannian metric g . In local coordinates the Christoffel symbols for the Levi-Civita connection are $\Gamma_{ij}^k = \frac{1}{2} g^{km} (\partial_i g_{mj} + \partial_j g_{mi} - \partial_m g_{ij})$ for $(i, j, k \in 1, \dots, d)$.

A second-order linear DS on \mathcal{M} can be expressed, for $t \in I \subset \mathbb{R}$, in intrinsic formulation as

$$\nabla_{v_\gamma} v_\gamma = \mathcal{F}(\gamma, v_\gamma, t)^\# = -d\phi^\# - D(\cdot, v_\gamma)^\#, \quad (2)$$

where $\gamma : I \rightarrow \mathcal{M}$ is a curve in the manifold \mathcal{M} , v_γ is the vector field generated by the tangent velocities of curve γ . On the right-hand side of Equation (2), \mathcal{F} is the total forces covector. It can be further split into elastic and dissipative components. Given a potential function, $\phi \in C^\infty(\mathcal{M})$, $d\phi^\#$ represents the elastic gradient field, while $D(\cdot, v_\gamma) \in T^*\mathcal{M}$ is the dissipative covector field. In local coordinates we have

$$(\nabla_{v_\gamma} v_\gamma)^k = -g^{ak} \partial_a \phi - D_m^k \dot{x}^m. \quad (3)$$

Combining Equations (1) and (3), we have

$$\underbrace{\ddot{x}^k}_{\ddot{\mathbf{x}}^k} + \underbrace{\Gamma_{ij}^k}_{\Xi_{ij}^k} \underbrace{\dot{x}^i \dot{x}^j}_{\dot{\mathbf{x}}^i \dot{\mathbf{x}}^j} = - \underbrace{g^{ak}}_{\mathbf{G}^{-1}} \underbrace{\partial_a \phi}_{\nabla \phi} - \underbrace{D_m^k}_{\mathbf{D}} \underbrace{\dot{x}^m}_{\dot{\mathbf{x}}^m}. \quad (4)$$

Note that $D_m^k = g^{ak} D_{am}$. Equation (4) can be expressed using vector notation as

$$\ddot{\mathbf{x}} = \mathbf{f}(\mathbf{x}, \dot{\mathbf{x}}) = -\mathbf{G}^{-1} \nabla \phi - \mathbf{D} \dot{\mathbf{x}} - \Xi \dot{\mathbf{x}}. \quad (5)$$

In the following sections, we will use capital bold letters to represent matrices in vector notation. When indices are used alongside a matrix, for the sake of clarity, the matrix itself will be denoted using capital letters without bold formatting.

4 Learning the Latent Manifold Embedding

Let \mathcal{M} and \mathcal{N} be two (non-compact) Riemannian manifolds, with respective charts (\mathcal{U}, x) and (\mathcal{V}, y) . We will indicate with g and h , the Riemannian metrics of \mathcal{M} and \mathcal{N} , respectively. In particular, for $\dim(\mathcal{M}) = d$, \mathcal{N} coincides with a $(d+1)$ -dimensional Euclidean space, \mathbb{R}^{d+1} . Therefore, $\mathcal{V} \equiv \mathbb{R}^{d+1}$ and $y \equiv id_{\mathbb{R}^{d+1}}$, where $id_{\mathbb{R}^{d+1}}$ is the identity map. Let $h = \delta_{ij}$ with respect to the chosen chart, where δ_{ij} is the Kronecker symbol, $\delta_{ij} = 1$ if $i = j$ otherwise $\delta_{ij} = 0$, and $i, j = 1, \dots, d+1$. With

$$\begin{array}{ccc} \mathcal{M} & \xrightarrow{f} & \mathcal{N} \equiv \mathbb{R}^{d+1} \\ \downarrow (\mathcal{U}, x) & & \downarrow (\mathcal{V} \equiv \mathbb{R}^{d+1}, y \equiv id_{\mathbb{R}^{d+1}}) \\ \mathbb{R}^d & \xrightarrow{y \circ f \circ x^{-1}} & \mathbb{R}^{d+1} \end{array}$$

Figure 2. Mapping structure across manifolds.

reference to Figure 2, $f : \mathcal{M} \hookrightarrow \mathbb{R}^{d+1}$ is a smooth isometric embedding into a $d+1$ Euclidean space. $(y \circ f \circ x^{-1})$ is the local coordinates expression of the embedding, i.e. the mapping between the two charts (\mathcal{U}, x) and (\mathcal{V}, y) .

We propose to model the components of the local coordinates formulation of the embedding as follows

$$(y \circ f \circ x^{-1})^i = \begin{cases} x^i & \text{if } i \leq \dim(\mathcal{M}) \\ \psi(x^i; \mathbf{w}) & \text{otherwise} \end{cases}, \quad (6)$$

where $\psi : \mathbb{R}^d \rightarrow \mathbb{R}$ is a smooth function parametrized by the weights \mathbf{w} and $\psi \in C^r(\mathbb{R}^d)$ with $r \geq 1$. We will refer to the embedding expressed in local coordinates with the vector notation $\Psi : \mathbb{R}^d \rightarrow \mathbb{R}^{d+1}$, highlighting the implicit dependence on ψ .

Proposition 1. $f : \mathcal{M} \rightarrow \mathbb{R}^{d+1}$ is a smooth mapping with local coordinates as in Equation (6). $f : \mathcal{M} \hookrightarrow \mathbb{R}^{d+1}$ is an embedding.

Proof. See Appendix A.1.

All the geometric operators, namely the metric and the Christoffel symbols, in Equation (5), are derived from the embedding defined in Equation (6) by leveraging on the pullback operation. In order to improve readability, in the following, we drop the explicit dependency of ψ on the local coordinates point \mathbf{x} and the weights \mathbf{w} . Nevertheless, all operators derived have to be considered dependent on \mathbf{x} and \mathbf{w} via ψ .

We first derive the metric as a function of the approximator ψ . The components of the pushforward map, $J_j^i = \partial_j (y \circ f \circ x^{-1})^i$, can be expressed in matrix notation as

$$\mathbf{J}(\mathbf{x}; \mathbf{w}) = \begin{bmatrix} \mathbf{I}^{\dim(\mathcal{M}) \times \dim(\mathcal{M})} \\ \nabla \psi^T \end{bmatrix}, \quad (7)$$

where $\nabla \psi = [\partial_1 \psi, \dots, \partial_{\dim(\mathcal{M})} \psi]^T$; \mathbf{J} is also known as the Jacobian. Isometry of the embedding implies that the metric on \mathcal{M} can be derived from the metric on \mathcal{N} via the pullback operation of the metric, $g = f^* h$. In local coordinates this can be expressed as

$$g_{ij} = \partial_i (y \circ f \circ x^{-1})^a h_{ab} \partial_j (y \circ f \circ x^{-1})^b. \quad (8)$$

Given $h_{ab} = \delta_{ab}$, Equation (8) can be written in matrix notation as

$$\mathbf{G}(\mathbf{x}; \mathbf{w}) = \mathbf{J}^T \mathbf{J} = \mathbf{I} + \nabla \psi \nabla \psi^T. \quad (9)$$

To derive the Christoffel symbols, we need to express the derivative of the metric. Given that the metric depends on \mathbf{x} only through the term $\nabla \psi \nabla \psi^T$, the Christoffel symbols (contracted with the velocity) can be expressed as

$$\Xi_j^q(\mathbf{x}, \dot{\mathbf{x}}; \mathbf{w}) = g^{qm} \frac{1}{2} \left(\partial_i (\partial_m \psi \partial_j \psi) + \partial_j (\partial_m \psi \partial_i \psi) - \partial_m (\partial_i \psi \partial_j \psi) \right) \dot{x}^i \quad (10)$$

The last two terms not yet defined in Equation (5) are the potential energy ϕ and the dissipative coefficients \mathbf{D} . We impose to the potential energy a classical quadratic structure $\phi = \frac{1}{2} \mathbf{x}^T \mathbf{K} \mathbf{x}$. Both the matrices \mathbf{K} and \mathbf{D} can be user-defined or left "open" for optimization.

Given the full state, $(\mathbf{x}, \dot{\mathbf{x}})$, of a DS, our training dataset is composed of position-velocity pairs $\{\mathbf{x}_m, \dot{\mathbf{x}}_m | m = 1, \dots, M\}$, with M the total number of sampled points. The ground truth is given by sampled acceleration $\{\ddot{\mathbf{x}}_m | m = 1, \dots, M\}$. We propose the following optimization problem

$$\min_{\mathbf{w}, \mathbf{K}, \mathbf{D}} \mathcal{F}_2(\mathbf{x}_m, \dot{\mathbf{x}}_m, \ddot{\mathbf{x}}_m | \mathbf{w}, \mathbf{K}, \mathbf{D}), \quad (11)$$

with

$$\begin{aligned} \mathcal{F}_2(\mathbf{x}_m, \dot{\mathbf{x}}_m, \ddot{\mathbf{x}}_m | \mathbf{w}, \mathbf{K}, \mathbf{D}) = & \\ & \sum_{m=1}^M \|\ddot{\mathbf{x}}_m + \mathbf{G}^{-1}(\mathbf{x}_m; \mathbf{w}) (\mathbf{K}(\mathbf{x}_m - \mathbf{x}^*) + \mathbf{D}\dot{\mathbf{x}}_m) + \\ & \Xi(\mathbf{x}_m, \dot{\mathbf{x}}_m; \mathbf{w}) \dot{\mathbf{x}}_m\|^2 + \lambda \|\mathbf{w}\|^2, \end{aligned} \quad (12)$$

where $\mathbf{K}, \mathbf{D} \in \mathcal{S}_{++}^d$, the manifold of Symmetric Positive Definite (SPD) matrices of dimension d . \mathbf{x}^* is the fixed stable equilibrium point, or attractor, of the DS. λ is a parameter weighing the regularization term. This parameter affects the manifold's curvature smoothness. Since the manifold's curvature translates into acceleration within the DS (via the Christoffel symbols), regularization plays a crucial role in containing high frequency change of curvature, avoiding high accelerations and potential overfitting.

SPD matrices optimization is achieved by parametrizing the generic SPD matrix as

$$\mathbf{M}(\boldsymbol{\alpha}, \boldsymbol{\xi}) = \mathbf{U}(\boldsymbol{\alpha}) \boldsymbol{\Lambda}(\boldsymbol{\xi}) \mathbf{U}(\boldsymbol{\alpha})^T, \quad (13)$$

with

$$\boldsymbol{\Lambda}(\boldsymbol{\xi}) = \begin{bmatrix} e^{\xi_1} & 0 & 0 \\ 0 & \ddots & 0 \\ 0 & 0 & e^{\xi_d} \end{bmatrix} \quad (14)$$

and \mathbf{U} the orthogonal matrix resulting from QR decomposition of the matrix constructed so to have the first column equal to the vector $\boldsymbol{\alpha} \in \mathbb{R}^d$. $\boldsymbol{\alpha}$ and $\boldsymbol{\xi}$ are the learnable parameters.

Theorem 1. Let $\mathbf{w} \in (-\infty, \infty)$. The dynamical system

$$\ddot{\mathbf{x}} = -\mathbf{G}^{-1}(\mathbf{x}; \mathbf{w}) (\mathbf{K}(\mathbf{x} - \mathbf{x}^*) + \mathbf{D}\dot{\mathbf{x}}) - \Xi(\mathbf{x}, \dot{\mathbf{x}}; \mathbf{w}) \dot{\mathbf{x}} \quad (15)$$

is globally asymptotically stable at the attractor \mathbf{x}^* , i.e. $\lim_{t \rightarrow \infty} \|\mathbf{x} - \mathbf{x}^*\| = 0$.

Proof. See Appendix A.2.

4.1 Gradient Systems & Incremental Learning

Our method can be applied to first order dynamics. Let $X : \mathcal{M} \rightarrow T\mathcal{M}$ be a vector field on \mathcal{M} . X is called a gradient system if

$$X = -d\phi^\# \xrightarrow{\text{local coordinates}} X^k = -g^{ik} \partial_i \phi. \quad (16)$$

As for the system in Equation (3), gradient systems are globally stable; moreover, they are globally exponentially stable. Such property follows from the fact that this type of systems are contracting on \mathcal{M} , [Simpson-Porco and Bullo \(2014\)](#), i.e. $g(\nabla_v X, v) \leq -\lambda g(v, v)$ for $p \in \mathcal{U}$ and $v \in T_p \mathcal{M}$. $\lambda > 0$ is the contraction rate. For strongly convex functions ϕ on \mathcal{U} , they satisfy the contraction condition $\text{Hess}(\phi) \succeq \lambda g$, where $\text{Hess}(\phi)$ is the Riemannian Hessian, see [Simpson-Porco and Bullo \(2014\)](#); [Wensing and Slotine \(2020\)](#) for details.

We can minimize the Mean Square Error (MSE) loss, as in Equation (11), having as target the sampled velocities

$$\min_{\mathbf{w}, \mathbf{K}} \sum_{m=1}^M \mathcal{F}_1(\mathbf{x}_m, \dot{\mathbf{x}}_m | \mathbf{w}, \mathbf{K}). \quad (17)$$

with

$$\mathcal{F}_1(\mathbf{x}_m, \dot{\mathbf{x}}_m | \mathbf{w}, \mathbf{K}) = \sum_{m=1}^M \|\dot{\mathbf{x}}_m + \mathbf{G}^{-1}(\mathbf{x}_m; \mathbf{w}) \mathbf{K}(\mathbf{x}_m - \mathbf{x}^*)\|^2 + \lambda \|\mathbf{w}\|^2, \quad (18)$$

If for simpler scenarios, first-order DS might suffice, more complicated cases require the usage of second-order DS. Nevertheless, first-order DS optimization can be performed as a way of finding a good initial solution for the second-order DS. As shown in Section 6.4, given the simple structure of a first-order DS, solution to Equation (17) can be found in considerably lower time than Equation (11). For complicated problems, this situation suggests to perform a sort of incremental learning: first, find optimal embedding weights, \mathbf{w}^* and stiffness matrix, \mathbf{K}^* , by solving repeatedly Equation (17); second, solve Equation (11) starting from \mathbf{w}^* and \mathbf{K}^* .

5 Online Kernel-Based Local Space Deformation

Kernel-based space deformation is an effective method for generating localized curvature, which subsequently influences the behavior of chart-based DS. As detailed in Section 5.1, for obstacle avoidance scenarios, this approach is particularly relevant to our method, where an explicit representation of the latent manifold is available.

Nevertheless, kernel-based deformation can also be adopted to model any type of global manifold's curvature realized as a linear combination of point-wise sources of the deformation. The analytical formulation provides a simplified framework that would allow us to gain intuition on the effect of the metric tensor and Christoffel symbols in the chart space DS, as curvature starts to appear in the manifold. These concepts are explored in Sections 5.2 and 5.3. Starting from a flat space scenario, we analyze the effect of locally deforming the space via Radial Basis

Function (RBF) kernels for first-order dynamics and second-order dynamics. In addition, for second-order dynamics, we show how it is possible to leverage on hybrid harmonic and geodesic motion to achieve concave obstacle avoidance, in fairly extreme scenarios, without recurring to planning strategies.

5.1 Obstacle Avoidance via Direct Space Deformation

One advantage of the proposed method is the direct extendibility to obstacle avoidance scenarios. We take advantage of the geometric obstacle avoidance techniques based on the local deformation or stretching of the space. In our approach, we encode the non-linearity of the DS within the curvature of the space. Without repeating the learning process, the non-linearity needed for the obstacle avoidance task can be encoded, locally, in the curvature of the space as well.

Geometry-based obstacle avoidance techniques rely on the definition of a metric that takes into account the presence of obstacles. The metric can be defined in the ambient space (and pulled back afterwards), [Beik-Mohammadi et al. \(2021\)](#), or directly in chart space, [Cheng et al. \(2020\)](#). The two approaches are equivalent. They work well if the original space on which the DS is taking place does not present pre-existent relevant curvature. In our approach, an explicit knowledge of the "shape" of the manifold is available. Given this knowledge, we show how it is possible to directly deform an already non-linear space to produce obstacle avoidance.

Let $k_{\text{chart}} : \mathbb{R}^d \times \mathbb{R}^d \rightarrow \mathbb{R}$ ($k_{\text{ambient}} : \mathbb{R}^{d+1} \times \mathbb{R}^{d+1} \rightarrow \mathbb{R}$) be a similarity measure in the chart (ambient) space. Let $\bar{\mathbf{x}} \in \mathbb{R}^d$ ($\bar{\mathbf{y}} \in \mathbb{R}^{d+1}$) be the location of an obstacle in chart (ambient) space. Given a current position $\mathbf{x} \in \mathbb{R}^d$ ($\mathbf{y} \in \mathbb{R}^{d+1}$), $k(\mathbf{x}, \bar{\mathbf{x}})$ ($k(\mathbf{y}, \bar{\mathbf{y}})$) informally expresses how close we are to the obstacle in the chart (ambient) space. Considering $\bar{\mathbf{x}}$ ($\bar{\mathbf{y}}$) fixed, we have $k_{\text{chart}}(\bar{\mathbf{x}}, \cdot) : \mathbb{R}^d \rightarrow \mathbb{R}$ ($k_{\text{ambient}}(\bar{\mathbf{y}}, \cdot) : \mathbb{R}^{d+1} \rightarrow \mathbb{R}$). We assume $k_{\text{chart}} \in C^r(\mathbb{R}^d)$ ($k_{\text{ambient}} \in C^r(\mathbb{R}^{d+1})$) with $r \geq 1$ and $k_{\text{chart}}(\mathbf{x}, \bar{\mathbf{x}}) \approx 0$ ($k_{\text{ambient}}(\mathbf{y}, \bar{\mathbf{y}}) \approx 0$) for $\|\mathbf{x} - \bar{\mathbf{x}}\| \geq \epsilon$ ($\|\mathbf{y} - \bar{\mathbf{y}}\| \geq \epsilon$) for some $\epsilon > 0$. The first condition imposes at least one time differentiability while the second one requires fast decay of the similarity measure away from the obstacle.

Recall in Equations (8) and (9), we assumed the ambient metric to be constant over all the space and equal to the identity, namely the Euclidean metric. We now use the following metric for the ambient Euclidean space

$$\mathbf{H} = \mathbf{I} + \nabla k_{\text{ambient}} \nabla k_{\text{ambient}}, \quad (19)$$

where $\nabla k_{\text{ambient}}$ expresses the derivative of the similarity measure k_{ambient} with respect to \mathbf{y} .

The metric in Equation (19) is implicitly defining a deformation of the ambient space. It can be derived via the pullback of the Euclidean metric of a $d+2$ -dimensional Euclidean space, embedding our ambient space $\Psi_{\text{ambient}} = [\mathbf{y}, k(\bar{\mathbf{y}}, \mathbf{y})]^T$. With $\mathbf{H} \in \mathbb{R}^{\dim(\mathcal{M})+1 \times \dim(\mathcal{M})+1}$, the chart space metric can be derived via the pullback of the ambient metric as in Equation (8), $\mathbf{G}(\mathbf{x}; \mathbf{w}) = \mathbf{J}^T \mathbf{H} \mathbf{J}$.

The pullback operation is equivalent to adding the "obstacle" metric to the chart space metric encoding the non-linearity of the DS, $\mathbf{G}_{\text{total}} = \mathbf{G}(\mathbf{x}; \mathbf{w}) + \mathbf{G}_{\text{obs}}$, where

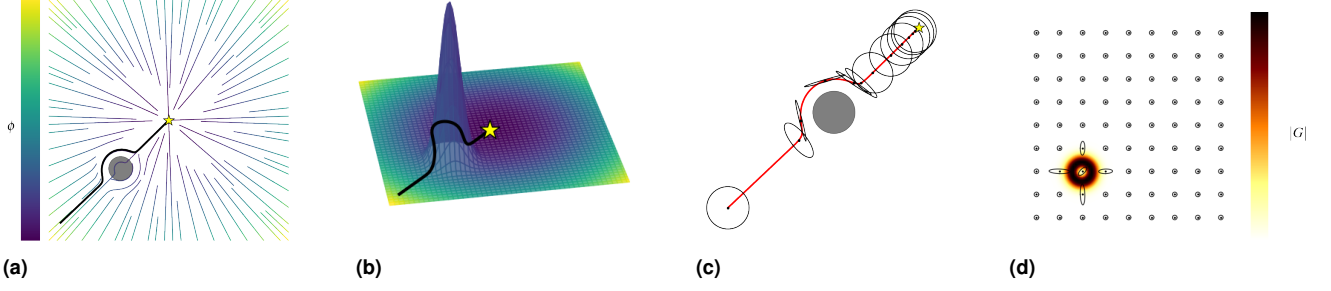


Figure 3. First-order DS in flat space with localized deformation in the obstacle area: (a) Vector field with one sampled streamline avoiding the obstacle; (b) 3D embedded representation of the manifold; (c) one sampled trajectory with eigenvalue decomposition ellipses of the inverse of the metric for selected location; (d) metric determinant function with eigenvalue decomposition ellipses of the metric.

$\mathbf{G}_{\text{obs}} = \mathbf{I} + \nabla k_{\text{chart}} \nabla k_{\text{chart}}^T$. Let $\mathbf{H} = \begin{bmatrix} \mathbf{I} + \mathbf{A} & \mathbf{B} \\ \mathbf{B}^T & 1 + \mathbf{C} \end{bmatrix}$, with $\mathbf{A} \equiv \nabla k_{\text{chart}} \nabla k_{\text{chart}}^T \in \mathbb{R}^{d \times d}$, $\mathbf{B} \in \mathbb{R}^{1 \times d}$ and $\mathbf{C} \in \mathbb{R}^{1 \times 1}$. The pullback operation in Equation (19) becomes $\mathbf{G} = \mathbf{I} + \mathbf{A} + \mathbf{B} \nabla \psi^T + \nabla \psi \mathbf{B}^T + \nabla \psi (\mathbf{I} + \mathbf{C}) \nabla \psi^T$. For $\gamma(t) \in \mathcal{M} \quad \forall t \geq 0$ we have $\mathbf{B}, \mathbf{C} = 0$; therefore $\mathbf{G} = \mathbf{I} + \mathbf{A} + \nabla \psi \nabla \psi^T = \mathbf{I} + \nabla k_{\text{chart}} \nabla k_{\text{chart}}^T + \nabla \psi \nabla \psi^T = \mathbf{G}_{\text{obs}} + \mathbf{G}(\mathbf{x}; \mathbf{w})$.

Adding metrics linearly is akin to treating the deformations of space, due to the non-linearity of the DS and the presence of an obstacle, separately. $\mathbf{G}(\mathbf{x}; \mathbf{w})$ is derived as in Equation (9) from the embedding Ψ in Equation (6); \mathbf{G}_{obs} can be derived from an embedding of the type $\Psi_{\text{obstacle}} = [\mathbf{x}, k(\bar{\mathbf{x}}, \mathbf{x})]^T$. In other terms, the deformation of the space due to the presence of the obstacle is agnostic of the previous curvature in the manifold. Such a scenario still yields good results where the space is fairly flat.

The explicit formulation of the embedding allows us to directly deform the space while actively taking into consideration the curvature of the space. Let $\{\bar{\mathbf{x}}_i, i = 1, \dots, N\}$ be the location of N obstacles in chart space; $\bar{\mathbf{w}}$ are the weights after learning the DS. We model obstacles as a kernel-based local deformation of the spaces given by

$$\bar{\psi}(\mathbf{x}) = \sum_{i=1}^N \eta_i k(\bar{\mathbf{x}}_i, \mathbf{x}), \quad (20)$$

where η_i is a user-defined weight assigned to the local deformation at $\bar{\mathbf{x}}_i$. At query-time the embedding in Equation (6) can be expanded as follows

$$\Psi = \begin{bmatrix} \mathbf{x} \\ \psi(\mathbf{x}; \bar{\mathbf{w}}) + \bar{\psi}(\mathbf{x}). \end{bmatrix} \quad (21)$$

The embedding in Equation (21) leads to the following pullback metric

$$\mathbf{G}(\mathbf{x}; \mathbf{w}) = \mathbf{I} + \nabla \psi \nabla \psi^T + \overbrace{2 \nabla \psi \nabla \bar{\psi}(\mathbf{x})^T}^{\text{coupling term}} + \nabla \bar{\psi}(\mathbf{x}) \nabla \bar{\psi}(\mathbf{x})^T. \quad (22)$$

The coupling term in Equation (22) encodes the pre-existent curvature of the space. Given the imposed condition on the regularity of k , both Proposition 1 and Theorem 1 still hold. The overall DS generated with such embedding retains global asymptotical stability, independently from the number of obstacles present.

Second order dynamical systems cannot perform proximal obstacle avoidance. Indeed, the geometrical term given by the Christoffel symbols generates forces that lead the system to "climb up" regions of local high-curvature, penetrating the obstacle. This forces conflict with the potential and dissipative ones— $\mathbf{G}^{-1} \nabla \phi$ and $\mathbf{D} \dot{\mathbf{x}}$ in Equation (5)—generating an overall motion that stagnates right after the obstacle. We refer the reader to Section 5.3 for more details and illustrations of these scenarios. This issue can be solved by introducing velocity-dependent local space deformations

$$\bar{\psi}(\mathbf{x}, \dot{\mathbf{x}}) = \sum_{i=1}^N \eta_i(\mathbf{x} - \bar{\mathbf{x}}_i, \dot{\mathbf{x}}) k(\bar{\mathbf{x}}_i, \mathbf{x}), \quad (23)$$

where $\eta_i(\mathbf{x} - \bar{\mathbf{x}}_i, \dot{\mathbf{x}})$ is framed as generalized sigmoid function acting on the cosine kernel between $\mathbf{x} - \bar{\mathbf{x}}_i$ and $\dot{\mathbf{x}}$

$$\eta_i(\mathbf{x} - \bar{\mathbf{x}}_i, \dot{\mathbf{x}}) = \frac{1}{1 + e^{-\tau(k_{\text{cos}}(\mathbf{x} - \bar{\mathbf{x}}_i, \dot{\mathbf{x}}) - \cos \theta_{ref})}}, \quad (24)$$

with $k_{\text{cos}}(\mathbf{x} - \bar{\mathbf{x}}_i, \dot{\mathbf{x}}) = \frac{(\mathbf{x} - \bar{\mathbf{x}}_i)^T \dot{\mathbf{x}}}{\|\mathbf{x} - \bar{\mathbf{x}}_i\| \|\dot{\mathbf{x}}\|}$. τ regulates the growth rate and θ_{ref} defines the starting growth point. Safe option can be $\theta_{ref} = \frac{\pi}{2}$. In this scenario, the underlying manifold dynamically deforms (locally) whenever the motion is monotonically decreasing towards the obstacle. If the system is moving away from the obstacle, the manifold curvature goes back to the flat or nominal state. This allows to effectively turn off the local geometrical terms once crossed the obstacle, allowing the system to reach the desired equilibrium point.

5.2 Local Space Deformation In First Order DS

Let the $d + 1$ embedding component $(y \circ f \circ x^{-1})^{d+1} = \psi$ be defined as a weighted sum of exponentially decaying kernels

$$\psi(\mathbf{x}) = \sum_{i=1}^N \alpha_i k(\mathbf{x}, \bar{\mathbf{x}}_i) = \sum_{i=1}^N \alpha_i \exp -\frac{\|\mathbf{x} - \bar{\mathbf{x}}_i\|^2}{2\sigma^2}, \quad (25)$$

where $\bar{\mathbf{x}}_i$ is the i -th kernel center and N is the number of kernel used. σ and α_i are user-defined parameters; the former

[‡]Note that this function, though dependent on \mathbf{x} , must be treated as constant in the derivation of the geometrical terms.

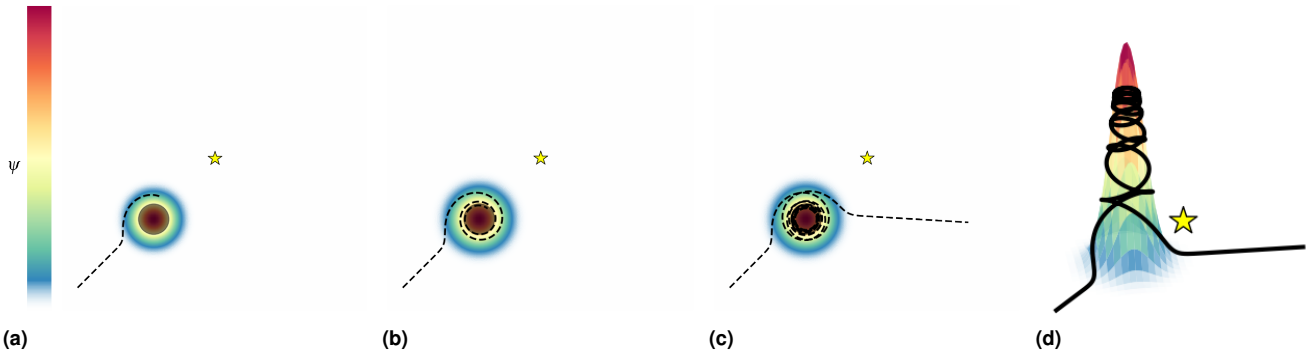


Figure 4. (a)-(c) Geodesic motion at time instants: 1s, 5s and 10s; (d) 3D embedded representation of case (c). In background the color gradient represents the $d+1$ embedding coordinate.

controls till which distant the local deformation affects the space geometry, the latter defines the magnitude of the deformation. In order to study the influence of a generic source of deformation, we consider $N = 1$ and $\alpha_1 = 1$.

Via the pull-back of the embedding metric we recover the metric onto the manifold. In case of Euclidean (identity) metric for the ambient space we have

$$\mathbf{G}(\mathbf{x}) = \mathbf{I} + \frac{1}{\sigma^4} (\mathbf{x} - \bar{\mathbf{x}})(\mathbf{x} - \bar{\mathbf{x}})^T k(\mathbf{x}, \bar{\mathbf{x}})^2. \quad (26)$$

See Appendix B.1 for derivation details. From Equation (26) we note that the metric tensor is composed by two terms: an identity term, independent from the location of the deformation source, and a term active only in the neighborhood of the deformation where $k(\mathbf{x}, \bar{\mathbf{x}})^2 \approx 1$. This

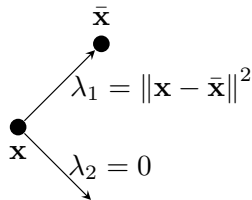


Figure 5. Kernel-based metric tensor eigenvalues and eigenvectors.

second term is given by the outer product of the distance vector between the current location and the source of the deformation. Outer product matrices are rank deficient with the eigenvector related to the only non-zero eigenvalues, $\lambda_1 = \|\mathbf{x} - \bar{\mathbf{x}}\|^2$, directed as $\mathbf{x} - \bar{\mathbf{x}}$.

Consider a 2D space locally deformed in $\bar{\mathbf{x}}$. Figure 5 shows the eigenvalues and the eigenvectors of the second term in the sum of Equation (26). Recall that the metric tensor is used to measure lengths. In the direction of the deformation source, the space elongates of an amount proportional to $\|\mathbf{x} - \bar{\mathbf{x}}\|^2 k(\mathbf{x}, \bar{\mathbf{x}})^2$. In the direction perpendicular to the deformation source, as expected, the space does not elongate; indeed, $\lambda_2 = 0$. The space is only stretched in the direction of the deformation source. This stretch reaches its maximum in the neighborhood of the source to than decrease gradually towards zero at $\bar{\mathbf{x}}$ where the space goes back to be flat, Figure 3d. This explains clearly how obstacle avoidance is achieved for a gradient system as in Equation (16). The projection of the gradient system's

velocity onto the inverse of the metric tensor decreases the velocity's component in the direction of the obstacle, located at the source of deformation, of an amount inversely proportional to the entity of space stretching. Figure 3c shows the ellipsoids generated by the inverse of the metric tensor. The velocity component perpendicular to the source of the deformation remains unchanged. This turns into an overall behavior of the gradient system that increases its velocity in the direction tangential to the obstacle. Note that, if the velocity of the gradient system, \mathbf{v} , points exactly towards the source of deformation, $\mathbf{v} \parallel \mathbf{x} - \bar{\mathbf{x}}$, the streamline will not be deflected at all. In such a case $\mathbf{v}^T (\mathbf{x} - \bar{\mathbf{x}})^\perp = 0$.

5.3 Local Space Deformation In Second Order DS

Second-order systems' behavior is affected by the Christoffel symbols. This term depends on the derivative of the metric tensor. As done for the differential of ψ , we can calculate the differential of the metric tensor

$$d\mathbf{G}(\mathbf{x})[\mathbf{v}] = \frac{1}{\sigma^4} \left((\mathbf{v}\tilde{\mathbf{x}}^T + \tilde{\mathbf{x}}\mathbf{v}^T)k(\tilde{\mathbf{x}}) + \frac{1}{\sigma^4} \tilde{\mathbf{x}}\tilde{\mathbf{x}}^T (\mathbf{v}^T \tilde{\mathbf{x}}\tilde{\mathbf{x}}^T \mathbf{v}) \right) k(\tilde{\mathbf{x}})^2. \quad (27)$$

where $\tilde{\mathbf{x}} = \mathbf{x} - \bar{\mathbf{x}}$, see Appendix B.2 for details. Consider a geodesic motion. The Christoffel symbol generates a deceleration perpendicular to the source of deformation.

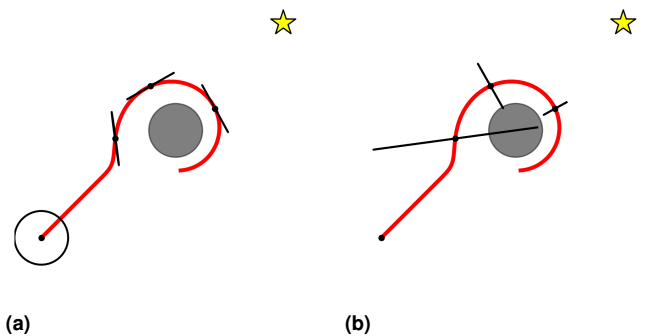


Figure 6. Geodesic motion after 1s with ellipses representing eigenvalues and eigenvectors of (a) the inverse of the metric and (b) the Christoffel symbols for selected locations.

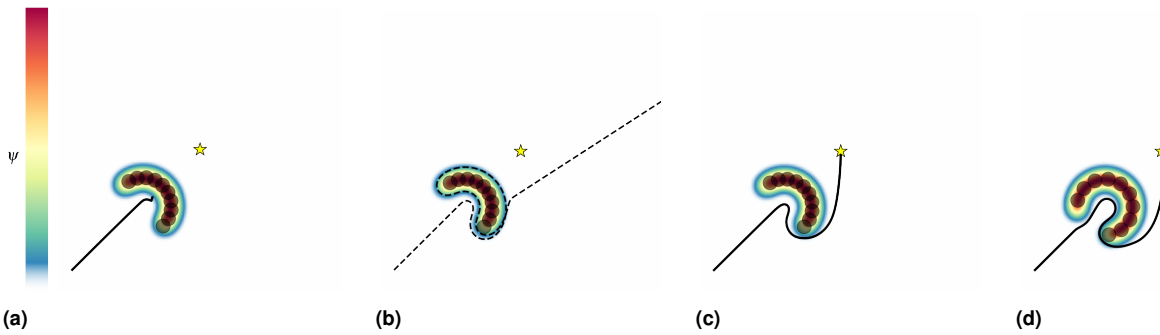


Figure 7. Concave obstacle avoidance: (a) harmonic motion; (b) geodesic motion; (c)-(d) hybrid motion for semicircle and horseshoe obstacles.

This, when approaching the source of deformation, deflects the streamlines avoiding the high curvature region. Nevertheless, if the streamline transits too close to the source of deformation, the geodesic gets captured by the high curvature region. Figures 4a to 4c show different frame of such geodesic motion. This is clear by analyzing the Christoffel symbols' principal components shown in Figure 6b. This components are perpendicular to the inverse metric ones, Figure 6a, and they generate an inward acceleration towards the obstacle that "captures" the geodesic motion leading the streamline to climb up and down the source of deformation as illustrated in Figure 6a.

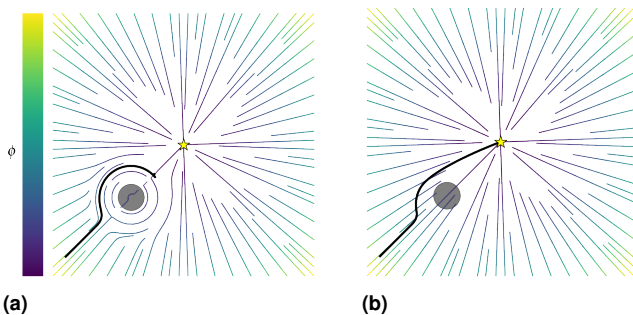


Figure 8. Second-order DS convex obstacle avoidance: (a) velocity independent local deformation; (b) velocity dependent deformation.

When adopting second-order DS, the harmonic part conflicts with the Christoffel symbol, generating a stagnation of the DS right after the obstacle, Figure 8a. In order to alleviate this issue, as seen in Section 5.1, it is possible to define a velocity-dependent local deformation, Equation (23). This makes the curvature of the space "dynamic", so that it disappears when the obstacle is surpassed. In this scenario, the effect of the Christoffel symbols, due to the local deformation, is canceled; the second-order DS behaves like a standard Euclidean harmonic oscillator, successfully reaching the attractor, Figure 8b. As a byproduct of this strategy, we obtained a more effective obstacle avoidance behavior. The DS shows an asymmetrical behavior before and after the obstacle, following the most efficient trajectory to reach the attractor once surpassed the obstacle.

Concave obstacle avoidance represents a more challenging scenario where both first and second order DSs will stagnates in the middle of obstacle due to conflicting forces, Figure 7a. Nevertheless, as seen previously, second-order

system geodesics exhibit the ability of navigating through the space deformation.

Similarly to what seen before, Figure 7b shows the geodesic motion in face of concave obstacle. When approaching the obstacle, the geodesic motion exhibits the ability of successfully avoid the deformed area. In order to perform concave obstacle avoidance, we propose an hybrid DS capable of leveraging on either geodesic or harmonic motion depending on the need

$$\ddot{\mathbf{x}} = -\Xi\dot{\mathbf{x}} - S(\bar{\psi}(\mathbf{x}, \dot{\mathbf{x}}))\mathbf{G}^{-1}(\mathbf{K}\mathbf{x} + \mathbf{D}\dot{\mathbf{x}}), \quad (28)$$

where $S(\cdot)$ is a generalized sigmoid function, as in Equation (24), to smoothly transition between harmonic and geodesic motion. Figures 7c and 7d, respectively for semicircle and horseshoe obstacle shape, show the behavior of the DS in Equation (28). The DS in Equation (28) exhibits geodesic behavior near to obstacle, when approaching it, $\sigma(\bar{\psi}(\mathbf{x}, \dot{\mathbf{x}})) \approx 0$. When leaving the obstacle, thanks to the velocity dependency introduced before, the DS exhibits harmonic behavior, given that $\sigma(\bar{\psi}(\mathbf{x}, \dot{\mathbf{x}})) \approx 1$, allowing to reach the attractor without being "captured" by the local deformation of the space.

6 Synthetic Example

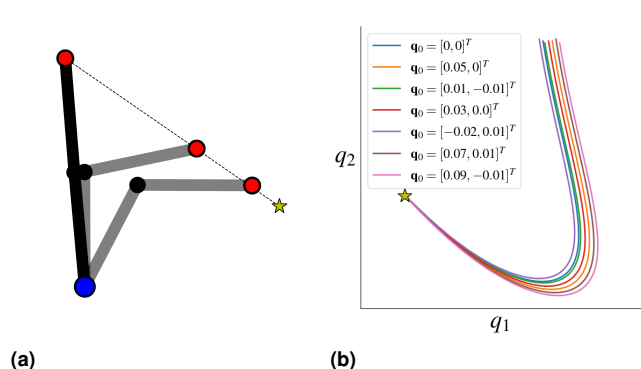


Figure 9. (a) 2-joints planar robotic arm performing a straight point-to-point motion of the end-effector; (b) corresponding trajectories in configuration space starting from different initial states.

In order to gain intuition on how the proposed method operates, in this Section, we start by analyzing a synthetic dataset achieved by gathering configuration space non-linear motions of a 2-joints planar robotic arm.

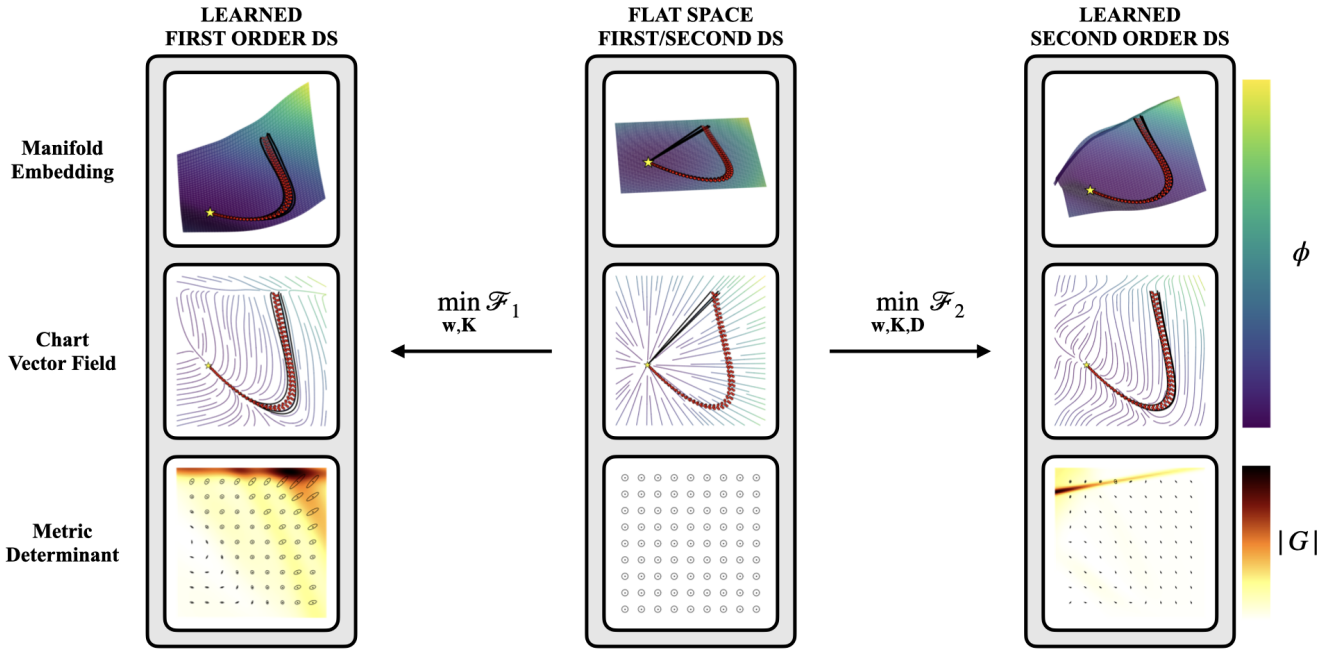


Figure 10. From top to bottom 3D embedded representation of the latent manifold, chart space representation of the DS field induced by the manifold curvature and metric tensor's determinant and ellipsoids for selected locations: (center) before learning; (left) learned first-order DS; (right) learned second-order DS.

Consider the 2-joints planar robotic arm in Figure 9a whose state is represented by the vector $\mathbf{q} = [q_1, q_2]^T$. Consider the generic equation of motion for a robotic arm, $\mathbf{M}(\mathbf{q})\ddot{\mathbf{q}} + \mathbf{C}(\mathbf{q}, \dot{\mathbf{q}})\dot{\mathbf{q}} = -\mathbf{g}(\mathbf{q}) + \boldsymbol{\tau}$, with $\mathbf{M}(\mathbf{q})$, $\mathbf{C}(\mathbf{q}, \dot{\mathbf{q}})$, $\mathbf{g}(\mathbf{q})$ and $\boldsymbol{\tau}$ being the inertia matrix, the Coriolis matrix, the gravity forces and input torques, respectively. We notice that classical mechanical systems are Riemannian geometries with the inertia matrix, $\mathbf{M}(\mathbf{q})$, playing the role of the metric tensor, $\mathbf{G}(\mathbf{q})$, and the fictitious (or Coriolis) forces, $\mathbf{C}(\mathbf{q}, \dot{\mathbf{q}})$, representing the geometric forces derived by the product of the Christoffel symbols and the velocities, $\boldsymbol{\Xi}(\mathbf{x}, \dot{\mathbf{x}})$. We elicit the non-linear dynamics of the robot by generating straight motions in the task (end-effector) space using operation space control, $\boldsymbol{\tau} = -\mathbf{J}(\mathbf{q})^T (\mathbf{K}(\mathbf{x} - \mathbf{x}^*) + \mathbf{D}\dot{\mathbf{x}})$, where $\mathbf{J}(\mathbf{q})$ is the Jacobian matrix relating joint space velocities to task space velocities, \mathbf{x}^* the equilibrium point in task space and \mathbf{K} and \mathbf{D} tunable gain matrices. Starting from different initial configurations, \mathbf{q}_0 , we generate in total 7 trajectories, Figure 9b, of which 4 are used for training and 3 for testing.

In order to learn the non-linear trajectories shown in Figure 9b, we approximate ψ , in Equation (6), with a feed-forward network composed by 2 hidden layers of 32 neurons each with hyperbolic tangent activation function to guarantee at least C^1 regularity; see Appendix C for details. The network's weights are randomly initialized very close to zero. This yields an almost flat manifold in the embedding space representation, Figure 10 central column in the top, with the metric tensor approaching the identity Euclidean metric. At the bottom of the central column, this is shown by the determinant of \mathbf{G} , the color gradient in background, and the ellipses representing the principal direction of the metric tensor. The determinant of the metric gives an absolute value of the local deformation of the space. In this case, the determinant of \mathbf{G} is constant and almost equal to 1 everywhere. In order to have an intuition of

the direction of the deformation, the ellipses generated by the eigen decomposition of the metric tensor are shown for selected location.

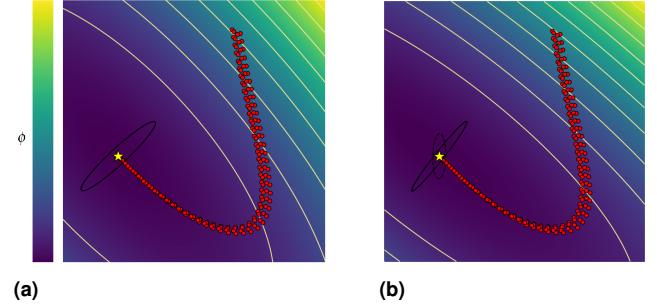


Figure 11. Learned potential function with stiffness and dissipation matrices principal direction ellipsoids for (a) first-order and (b) second-order DS.

For the Euclidean metric generated by the almost flat space condition, such ellipses approach the shape of a circle. For the first order DS learning, we start from a spherical stiffness matrix. For the second order DS, we additionally set the damping matrix to yield an initial critically damped behavior in flat space, $\mathbf{D} = 2(\mathbf{KM})^{1/2}$. These conditions, for both DSs, results in a linear vector field, in the chart space representation, where the sampled streamlines are straight lines towards the attractor, in the middle of the central column in Figure 10. Note that, for the second-order DS, the vector field is obtained by integrating one step forward Equation (4), considering an initial velocity of zero. During the training process, the stiffness and the damping matrices can be spherical, diagonal or Symmetric Positive Definite (SPD), as well as fixed and therefore not considered as an optimization variable. The stiffness

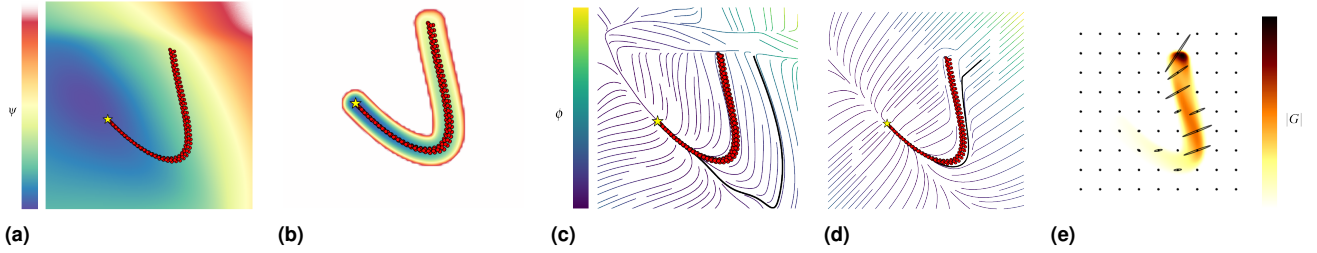


Figure 12. (a) Gradient of the $d+1$ embedding component; (b) gradient of the $d+1$ embedding component with bump function; (c) one sampled trajectory with initial position far away from the demonstrated trajectories; (d) one sampled trajectory with initial position far away from the demonstrated trajectories with bump function; (e) metric determinant with eigenvalue decomposition ellipses of the metric from selected location.

and dissipation matrices, together with the curvature of the manifold, contribute to the non-linearity of the learned DS.

Figures 11a and 11b show the isoline of the potential function, after the learning, for the first and second order DS. In this example, we opted for an SPD matrix for both the stiffness and the damping matrices. Observe that in both cases, first and second order DS, the learnt stiffness matrix "aligns" itself orthogonally to the direction of demonstrated trajectories in the neighborhoods of the attractor. Therefore, part of the contribution to the non-linearity of the streamlines is outsourced to the potential function gradient. The remaining non-linearity needed for learning the demonstrated DS is taken over by the curvature of the space.

The top row of Figure 10 shows the embedded representation of the learnt manifold for the first (left column) and second (right column) order DS. In the bottom line, the behavior of the determinant of the metric for both DSs. In the case of the first-order DS, the curvature of the space gives rise to an *energetic barrier* at the onset of the trajectory, guiding the flow downward. In the lower-right region of the space, it steers the streamlines towards the attractor. This phenomenon is further elucidated by examining the principal directions indicated by the ellipses of the metric tensor. The ellipses experience a compression perpendicular to the direction of maximal deformation. As a consequence, this leads to a projection of DS velocities tangentially to the deformation of the space, resulting in the desired non-linearity. In the case of the second-order DS shown at the bottom, we encounter a similar scenario, but this time with a more pronounced energetic barrier in the lower region of the space. This barrier, via the Christoffel symbols, induces directional deceleration, effectively guiding the streamlines towards the attractor.

The resulting chart space representation of the vector field along with 3 sampled testing trajectories is shown in the central row. The underlying deformation of the space induces an apparent non-linearity in the chart space representation of both DSs. The streamlines curve, adapting to the shape of the demonstrated trajectory for the first-order DS. Differently, in the second-order DS, the sampled streamlines do not evolve accordingly to the background vector field. Indeed, for the second-order DS, the background vector field assumes in each point zero initial velocity.

Consider the first order DS. Figure 13a shows how the principal directions of the inverse metric tensor vary along

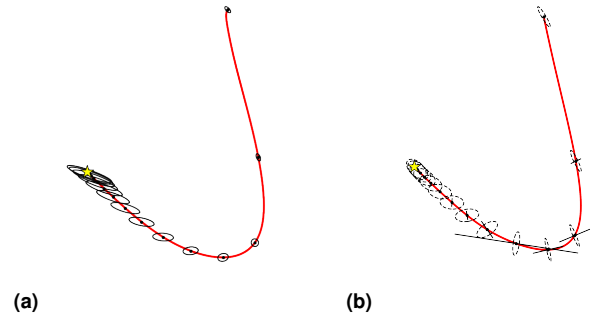


Figure 13. Evolution of (a) inverse metric and (b) Christoffel symbols principal directions along one sampled streamline.

the one sampled trajectory due to deformation of the space. In the first part of the trajectory the ellipses are considerably elongated in q_1 . By projecting the DS current velocity onto the inverse metric principal axis, see Equation (16), the velocity of the DS increases in the direction of q_1 , generating the non-linear behavior depicted. Similar consideration, Figure 13b, can be done for the second-order DS by analyzing the Christoffel symbols (solid line) and metric tensor inverse (dashed line) ellipses.

Notice that the DS is linear on the manifold and follows a mass-spring-damper system as in Equation (5). The curvature of the manifold makes the DS appear non-linear in the chart (Euclidean) space representation of the manifold.

6.1 Locally Active Space Deformation

Despite global stability guarantees, when using global function approximator such as neural networks, the behavior far away from demonstrations is not predictable. Figure 12a shows the contour of the $d+1$ embedding component, approximated by a neural network, that directly influences the curvature of the manifold. Close to the demonstrated trajectories, the function approximator ensures that the manifold's curvature would yield the desired DS non-linearity. Away from the demonstrated trajectories, the local curvature of the manifold produces a DS behavior that can be sub-optimal or even undesired, see Figure 12c.

In order to alleviate this problem, we propose to flatten the space far away from the demonstrations. This is operation is performed at query time and it does not influence the training process. In this case, by flattening the space away from the

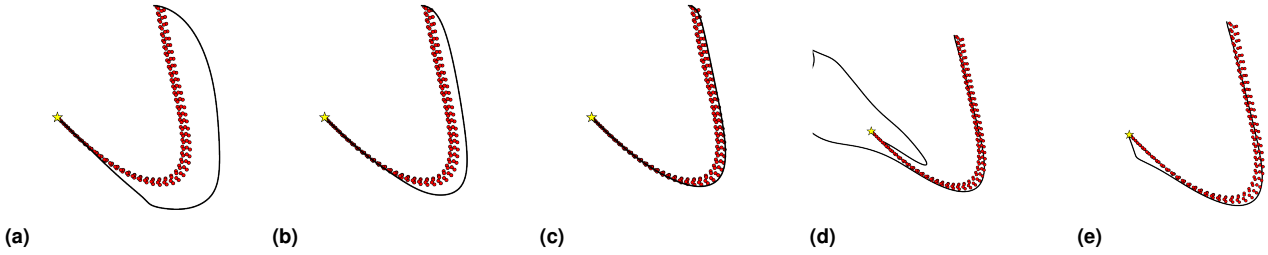


Figure 14. Second-order DS (a) without, (b)-(c) with ($\lambda = 10$ and $\lambda = 20$) directional dissipation. Second-order DS (d) without and (e) with exponential dissipation.

demonstrations, the DS will exhibit global linear behavior except for the regions where training points are available. The nominal behavior far away from the demonstration is not limited to be linear. By choosing different types of nominal curvature, the DS will exhibit different behaviors.

To enforce flat space behavior in those areas where training data is not available, we deploy a distance dependent bump function. Let \mathcal{X} denoting the training set. We define

$$\psi_{\text{bumped}}(\mathbf{x}; \mathbf{w}) = \alpha(\mathbf{x})\psi(\mathbf{x}; \mathbf{w}), \quad (29)$$

where $\alpha(\mathbf{x})$ is a bump function defined as

$$\alpha(\mathbf{x}) = \begin{cases} \frac{1}{e} \exp\left(-\frac{r^2}{r^2 - \text{dist}(\mathbf{x}, \mathcal{X})^2}\right), & \text{dist}(\mathbf{x}, \mathcal{X}) \leq r \\ 0, & \text{otherwise.} \end{cases} \quad (30)$$

$\text{dist}(\mathbf{x}, \mathcal{X})$ is the distance between \mathbf{x} and its nearest neighborhood $\mathbf{x}_i \in \mathcal{X}$.[§] r is a user-defined parameter that regulates how far from the demonstrated trajectories the manifold should start to have nominal zero curvature.

Figure 12b shows the third embedding component behavior when pre-multiplied by the bumped function. The manifold region in the neighborhood of the demonstration preserves its original curvature given by the learning procedure. Away from the demonstration the manifold becomes increasingly flat. This type of manifold structure yields a linear behavior away from the demonstrations that smoothly transitions towards nonlinear behavior when approaching the area of the demonstrated trajectories, see Figure 12d. By analyzing the determinant of the metric tensor, Figure 12e, we can clearly notice how this type of embedding structure affects the curvature only in localized portion of the space. The ellipses of the metric tensor away from the demonstrated trajectories converge to circles; constant and equal eigenvalues of value 1. Close to the demonstrations the ellipses deform, yielding the correct geometric accelerations to follow the demonstrated trajectories.

6.2 Directional & Exponential Dissipation

Second-order DSs offer a richer and more versatile way to articulate high-level policies compared to first-order DS. However, their application in LfD is uncommon. Primarily, user demonstrations tend to emphasize position over velocity. For instance, during a kinaesthetic demonstration with a robot—manually guiding the robot’s end-effector along a desired path—focus is primarily on the sequence of positions rather than the end-effector’s velocity. Consequently,

this oversight can result in unintended behaviors near the demonstrated positions, especially when the state velocity differs from the demonstrated one. In this section, we present two potential strategies aimed at mitigating this issue when deploying second-order DSs.

Figure 14a shows the streamline sampled from the initial position of one of the testing trajectories. In this case the initial velocity is not equal to zero, differently from what we had during the training. As it is possible to see in this scenario, the sampled streamline does not follow at all the demonstrations taking an alternative path to reach the attractor. When controlling, for instance, on real robot’s end-effector, we cannot ensure the current velocity of the end-effector will always lie to the demonstrated ones for each specific position, especially when the controlled system has to answer to compliance requisite in the interaction with humans. In order to make second-order DS reliable in this type of scenario and alleviate undesired behaviors whenever we have initial velocities far away from the demonstrated ones, we propose to add, without loss of stability, an additional directional dissipation

$$\ddot{\mathbf{x}} = -\mathbf{G}^{-1}(\mathbf{x}; \mathbf{w}) (\mathbf{K}(\mathbf{x} - \mathbf{x}^*) + \mathbf{D}\dot{\mathbf{x}}) - \Xi(\mathbf{x}, \dot{\mathbf{x}}; \mathbf{w})\dot{\mathbf{x}} - \lambda_{\text{dir}} \left(\frac{\dot{\mathbf{x}}}{\|\dot{\mathbf{x}}\|} - \frac{\dot{\mathbf{x}}^*}{\|\dot{\mathbf{x}}^*\|} \right). \quad (31)$$

$\dot{\mathbf{x}}^*$ is a first-order reference DS, providing the desired velocity field nominal behavior. Whenever first-order DS following the demonstrated trajectories is available we can take advantage of it in order to steer our second-order DS within the demonstrated velocities. Figures 14b and 14c show the resulting streamline for increasing values of λ_{dir} .

Another issue encountered in adopting second-order DS is the undesired under-damped behavior shown in Figure 14d. If for classical harmonic damped oscillator we can easily set the damping term so to have a critically-damped behavior, this is not possible for oscillators on manifolds whereas the Christoffel symbols acts as a non-linear damping term not under our control. This leads to trajectory overshoot in the

[§]In order to increase regularity of the $\psi_{\text{bumped}}(\mathbf{x}; \mathbf{w})$, $\text{dist}(\mathbf{x}, \mathcal{X})$ can be computed as the average distance between \mathbf{x} and its K nearest neighborhoods. This is still computationally cheap by adopting modern efficient implementation of KNN. Distribution based bump function may represent an alternative way to KNN. In this case the distribution can be learned offline (for instance via GMM) yielding almost zero cost at query time. In addition joint position-velocity distribution could be learned to enforce flat-space behavior away from the demonstrated velocities.

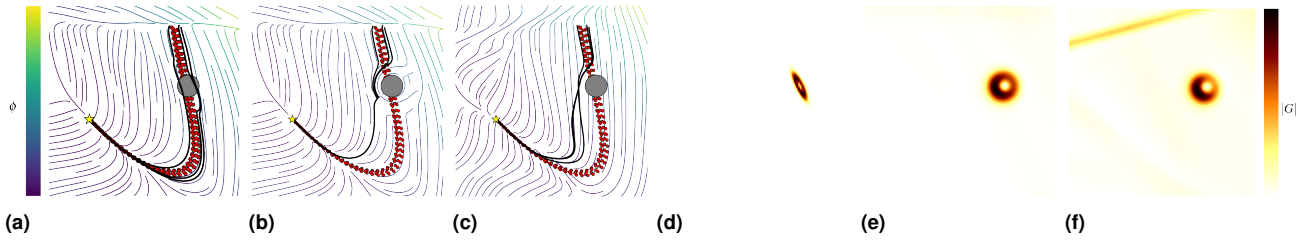


Figure 15. Vector field and metric determinant for (a)-(d) first-order DS with classic method; (b)-(e) first-order DS with direct deformation method; (c)-(f) second-order DS with direct deformation method.

attractor area. In order to alleviate this problem, an additional dissipative force can be considered

$$\begin{aligned} \ddot{\mathbf{x}} = & -\mathbf{G}^{-1}(\mathbf{x}; \mathbf{w}) (\mathbf{K}(\mathbf{x} - \mathbf{x}^*) + \mathbf{D}\dot{\mathbf{x}}) - \Xi(\mathbf{x}, \dot{\mathbf{x}}; \mathbf{w})\dot{\mathbf{x}} \\ & - \lambda_{\text{exp}} \exp\left(-\tau\|\mathbf{x} - \mathbf{x}^*\|^2\right). \end{aligned} \quad (32)$$

This new dissipative force acts only locally and it grows exponentially approaching the attractor. As shown in Figure 14e this term effectively arrest the DS streamline at the attractor removing the problem of overshooting.

6.3 Obstacle Avoidance Online Direct Deformation

We now show how the learned DS can adapt to the presence of obstacles. As analyzed in Section 5.1 we have two ways of performing obstacle avoidance leveraging on the geometrical structure of the space.

The first method, as in Beik-Mohammadi et al. (2021), consists in designing a specific metric that acts in the ambient space. All the geometric terms are then derived as shown in Section 4 with $\mathbf{H} = \hat{\mathbf{H}} \neq \mathbf{I}$. We will refer to this approach as *classical method*.

In our framework, we have the additional and more intuitive option of directly deforming the space by altering locally the embedding map post-training, $\hat{\psi}(\mathbf{x}; \bar{\mathbf{w}}) = \psi(\mathbf{x}; \bar{\mathbf{w}}) + \bar{\psi}(\mathbf{x})$. We will refer to our approach as *direct deformation method*.

For the classical method we opt, as barrier function, for the Gaussian kernels given by $k(\bar{\mathbf{y}}, \mathbf{y}) = \exp\left(-\frac{\|\bar{\mathbf{y}} - \mathbf{y}\|^2}{2\sigma^2}\right)$, with kernel width σ . $\bar{\mathbf{y}} = \Psi(\bar{\mathbf{x}})$ is the obstacle position in the ambient space. The ambient metric is then constructed as in Equation (19).

For the direct deformation of the space the same Gaussian kernel acting in the chart space $k(\bar{\mathbf{x}}, \mathbf{x})$ can be used, with no need to query the ambient space location of the obstacle. The embedding is then altered as in Equation (21).

σ is a user-defined parameter regulating the speed of the decay of the local deformation. One straightforward way of setting this parameter is imposing the desired decay at the border of the obstacle. For instance $\sigma = \sqrt{-\frac{1}{2} \frac{r^2}{\log \epsilon}}$, where r is the local radius of the obstacle and ϵ is value of the kernel at r ; typically $\epsilon \leq 1e-3$. Barrier functions of the type $k(\bar{\mathbf{y}}, \mathbf{y}) = \exp\left(\frac{a}{b(\|\bar{\mathbf{y}} - \mathbf{y}\| - r)^b}\right)$ can be used as well. a and b are user-defined parameters that regulate the entity of the local deformation of the space and r is the radius of the obstacle as before.

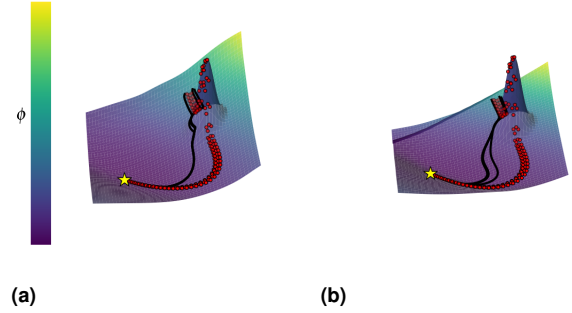


Figure 16. Embedding space visualization of the local deformation due to the obstacle presence for (a) first-order DS and (b) second-order DS.

The training process is carried out using $\mathbf{H} = \mathbf{I}$ and $\hat{\psi}(\mathbf{x}; \bar{\mathbf{w}}) = \psi(\mathbf{x}; \bar{\mathbf{w}})$. The ambient metric, for the classical method, and the embedding map, for the direct deformation method, will be locally modified at test time to take into account the presence of obstacles.

Figure 15a shows, for the first order DS, the resulting vector field and test sampled trajectories, adopting the classical method for performing obstacle avoidance. In this scenario, it is possible to notice how the streamline do not avoid the obstacle properly. Moreover, by looking at Figure 15d, we can notice how the space has been deformed in a asymmetric way. Despite the isotropic kernel used, the local deformation of the space spans a tilted elliptic area. This is due to the presence of prior curvature in the embedded space given by the learnt DS. Whenever considerable curvature is present in the manifold, the lack of the coupling term, see Equation (22), can lead to undesired behavior in the neighborhood of the obstacle.

By considering the obstacle as a direct local deformation of the manifold, we recover the expected behavior of the vector field in the neighborhood of the obstacle, Figure 15b. The metric determinant, Figure 15e, displays space deformation consonant with the isotropic kernel used. The same happens for a second-order DS, Figures 15c and 15f. Differently from the first-order DS, as already observed already in Section 5.3, we notice how the streamlines detach more quickly from the obstacle showing asymmetric behavior before and after the local deformation.

In this case, we can directly visualize how the presence of the obstacle affects the manifold's curvature, Figures 16a and 16b. The manifold structure is not re-learned and it remains globally consistent with the embedded

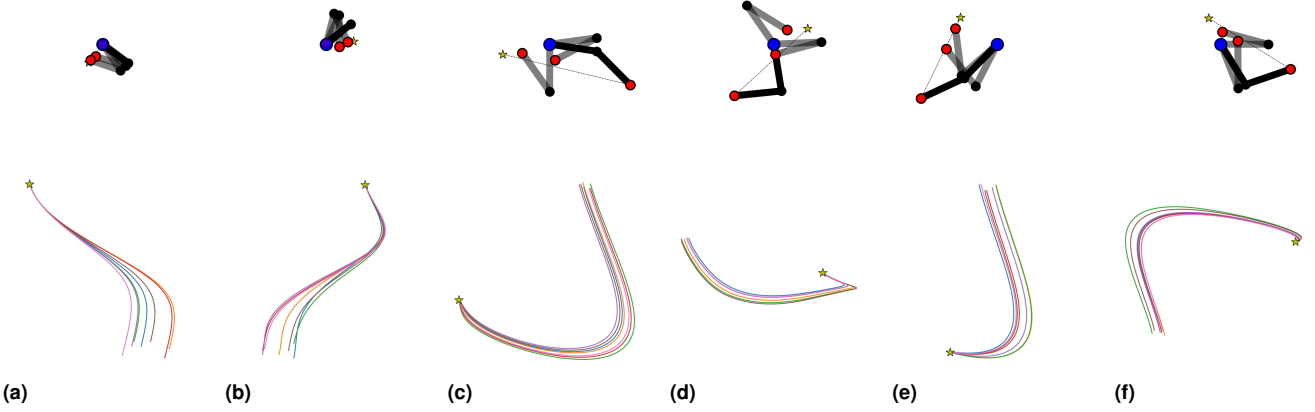


Figure 17. Evaluation: (top) Motion frames of 2-joints planar robotic manipulator; (bottom) sampled DSs in configuration space, corresponding to the above depicted robotic motion.

representation shown in Figure 10. The obstacle affects the geometry only locally allowing the streamlines to follow the demonstrated trajectories away from the obstacle.

6.4 Evaluation

In order to evaluate the performance of the learned DS we employ three metrics: 1) Root Mean Square Error, $RMSE = \sqrt{\frac{1}{M} \sum_{i=1}^M \|\dot{\mathbf{x}}_i^{\text{ref}} - \dot{\mathbf{x}}_i^{\text{DS}}\|^2}$, 2) Cosine Similarity, $CS = \frac{1}{M} \sum_{i=1}^M \left| 1 - \frac{\langle \dot{\mathbf{x}}_i^{\text{ref}}, \dot{\mathbf{x}}_i^{\text{DS}} \rangle}{\|\dot{\mathbf{x}}_i^{\text{ref}}\| \|\dot{\mathbf{x}}_i^{\text{DS}}\|} \right|$, and 3) Dynamic Time Warping Distance, DTWD. (1) and (2) are point-wise metrics that measure the similarity between two vector fields; in the first case, magnitude and direction are considered while, in the second case, only direction influences the score.

For the first order system we have $\dot{\mathbf{x}}_i^{\text{DS}} = \mathbf{f}(\mathbf{x}_i^{\text{ref}})$. In order to compare first and second order systems with metric (1) and (2), for the second order system, we sample one step forward from the learned DS with initial condition given by $(\mathbf{x}_i^{\text{ref}}, \dot{\mathbf{x}}_i^{\text{ref}})$. Using the same sampling frequency, h , of the testing trajectories we have

$$\dot{\mathbf{x}}_{i+1}^{\text{DS}} = \dot{\mathbf{x}}_i^{\text{ref}} + \frac{1}{h} \mathbf{f}(\mathbf{x}_i^{\text{ref}}, \dot{\mathbf{x}}_i^{\text{ref}}) \quad \text{for } i = 1, \dots, N-1, \quad (33)$$

where N the number of sampled points per testing trajectory.

(3) measures the dissimilarity between the shape of a reference trajectory and its corresponding reproduction from the same initial points (and velocity for second order systems). In this case, for each testing trajectory, we sample a streamline starting from initial condition $\mathbf{x}_1^{\text{ref}}$, for the first order DS, and $(\mathbf{x}_1^{\text{ref}}, \dot{\mathbf{x}}_1^{\text{ref}})$, for the second order DS, with

sampling frequency h . The sampling frequency is coincident with the one used to sample the testing trajectories.

We compare our approach against the learning dynamical systems via diffeomorphism in Rana et al. (2020). We refer to this approach as *Euclideanizing Flows* (EF)[¶]. This approach adopts an NVP transformation structure, Dinh et al. (2016), where the diffeomorphism is achieved by a sequence of the so-called *coupling layers*. Each coupling layers is composed by operations of scaling and translation approximated by weighted sum of Random Fourier Features (RFF), Rahimi and Recht (2007), kernels.

In each scenario, we conduct Adam optimization until convergence with a dynamic learning rate starting from a value of 0.01. We use a single NVIDIA GeForce 3090-24GB GPU for the experiments. Each trajectory is constituted by triplets $\{\mathbf{x}_i, \dot{\mathbf{x}}_i, \ddot{\mathbf{x}}_i\}_{i=1, \dots, T}$ with $T = 1000$.

Figure 17 the different DSs on which we conducted our evaluation. For each DS we performed 5 training repetitions, each time randomizing training and testing trajectories. Table 1 reports the comparison of our approach for first and second order DS against the baseline. Our method for the first-order DS achieves on average better performance than the baseline. For the second-order DS, our approach outperforms by a considerable margin the baseline and the first-order DS in RMSE.

Table 2 reports, over 2000 iterations, the training loss and time for each of the tested approaches. Due to the simplicity

[¶]Efficient PyTorch-based implementation of EF available at:

<https://github.com/nash169/learn-diffeomorphism>

Demonstration	RMSE [rad/s]			CS [rad]			DTWD [rad ²]		
	Baseline	1st - DS	2nd - DS	Baseline	1st - DS	2nd - DS	Baseline	1st - DS	2nd - DS
(a)	1.35 ± 0.66	0.40 ± 0.20	0.02 ± 0.00	0.04 ± 0.03	0.01 ± 0.00	0.01 ± 0.00	1.04 ± 0.89	0.20 ± 0.16	0.15 ± 0.06
(b)	6.81 ± 3.10	0.30 ± 0.07	0.02 ± 0.00	0.37 ± 0.25	0.01 ± 0.00	0.01 ± 0.00	2.57 ± 1.10	0.28 ± 0.07	0.70 ± 0.24
(c)	> 10.00	1.31 ± 0.13	0.04 ± 0.01	0.49 ± 0.44	0.01 ± 0.00	0.00 ± 0.00	> 10.00	1.59 ± 0.31	1.19 ± 0.26
(d)	> 10.00	1.25 ± 0.07	0.05 ± 0.01	0.71 ± 0.31	0.02 ± 0.00	0.00 ± 0.00	> 10.00	3.15 ± 0.57	2.33 ± 0.18
(e)	4.17 ± 2.79	0.72 ± 0.11	0.02 ± 0.00	0.03 ± 0.01	0.00 ± 0.00	0.00 ± 0.00	1.21 ± 0.48	0.26 ± 0.11	0.31 ± 0.10
(f)	> 10.00	0.88 ± 0.11	0.03 ± 0.00	0.49 ± 0.33	0.01 ± 0.00	0.00 ± 0.00	7.45 ± 5.28	5.17 ± 5.65	1.04 ± 0.45

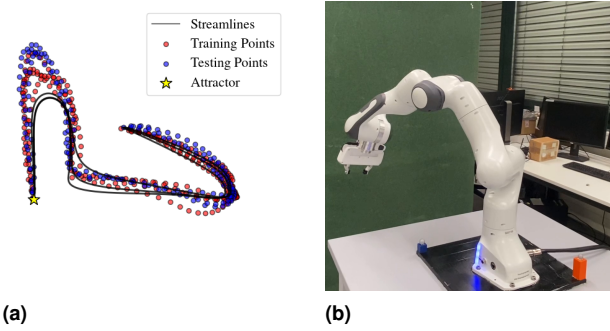
Table 1. Evaluation results: for each sampled DS in Figure 17 we evaluate 1st and 2nd order learning DS against the Baseline with respect to the three metrics RMSE, Cosine Similarity Kernel in velocity space, DTWD.

	Baseline	First DS	Second DS
Loss	6.8e-4 ± 9.6e-4	8.7e-5 ± 2.2e-5	1.1e-3 ± 8.5e-4
Time/Epoch	0.017 ± 8.7e-5	0.003 ± 1.9e-4	0.011 ± 1.2e-4
Train Epochs	4404.3 ± 1744.9	4168.3 ± 797.3	13257.0 ± 2280.3

Table 2. Training results.

of our architecture, our method can be up to 5 times faster than the baseline for the first-order DS. Despite the increased complexity of the learning problem with respect to the first-order case, our method still manages to be up to two times faster at training time with respect to the baseline.

7 Robotics Experiments

**Figure 18.** Learning three dimensional Dynamical Systems for Robotic Arm Control.

We evaluate our method on learning 3D robotic end-effector motions in real-world settings[†].

The robotic platform used consists of the 7-DOF Franka Emila, Figure 18b. We gather 7 samples of the desired task space behavior by manually driving the robot’s end-effector. 4 trajectories are selected for training; the remaining trajectories are used as testing set. Figure 18a shows, qualitatively, the 3D learnt DS. The red dots represent the the sampled observations from the demonstrated trajectories converging towards the attractor represented by the yellow star. The blue trajectories represents the streamlines obtained by sampling, till convergence, from the learnt 3D DS starting from two different initial locations.

The equations of motion for an articulated robot system can be described as

$$\mathbf{M}(\mathbf{q})\ddot{\mathbf{q}} + \mathbf{h}(\mathbf{q}, \dot{\mathbf{q}}) = \boldsymbol{\tau}_c + \boldsymbol{\tau}_e \quad (34)$$

where $\mathbf{M}(\mathbf{q})$ is the inertia matrix, $\mathbf{h}(\mathbf{q}, \dot{\mathbf{q}})$ is the sum of gravitational, centrifugal and Coriolis forces. $\boldsymbol{\tau}_c$ and $\boldsymbol{\tau}_e$ are the vector of controlled and external joint torques, respectively.

Robustness to spatial and temporal perturbation as well as compliancy in the event of human interactions are the desired features of our control strategy. In this work, we test three different torque-based control strategies. Figure 19a illustrates the generic control strategy where robot configuration space state is fed directly to the controller module while task space information are pre-processed by the learned DS before going inside the controller. Depending on the DS order we have different control strategies illustrated in details in Figure 19b. The left block shows

the two DS tested. Both the first-order and second-order DSs are split in two submodules, one operating in \mathbb{R}^3 and the other one in $SO(3)$, respectively used to control end-effector’s position and orientation. The DS operating in \mathbb{R}^3 is learned based on the demonstrated trajectory. The DS operating in $SO(3)$ generates a linear DS (critically damped for the second-order space) with the velocities taking place in the Lie Algebra $\mathfrak{so3}$, Solà et al. (2021).

Passive Interaction Control Model-free control strategy that naturally adapts DS-based control, Kronander and Billard (2016). It is constitute by a feedback controller with solely the damping term

$$\boldsymbol{\tau}_c = \mathbf{J}^T \mathbf{D}(\dot{\mathbf{x}} - \mathbf{f}(\mathbf{x})) + g(\mathbf{q}). \quad (35)$$

$\mathbf{f}(\mathbf{x})$ is the target velocity generated by the first-order DS, top-left in Figure 19b.

Model-Free Quadratic Programming Control In model-free QP control we first find the desired joint velocities as a solution of the optimization problem

$$\begin{aligned} \min_{\dot{\mathbf{q}}, \boldsymbol{\xi}} \quad & \frac{1}{2} \dot{\mathbf{q}}^T \mathbf{Q} \dot{\mathbf{q}} + \boldsymbol{\xi}^T \mathbf{W} \boldsymbol{\xi} \\ \text{s.t.} \quad & \mathbf{J} \dot{\mathbf{q}} = \mathbf{f}(\mathbf{x}) + \boldsymbol{\xi} \\ & \mathbf{q}^- \leq \mathbf{q}_{t-1} + dt \dot{\mathbf{q}} \leq \mathbf{q}^+ \\ & \dot{\mathbf{q}}^- \leq \dot{\mathbf{q}} \leq \dot{\mathbf{q}}^+. \end{aligned} \quad (36)$$

The target task space velocity generate by the first-order DS is imposed as relaxed inverse kinematics constraint in the optimization problem. After prior integration of the desired joint velocities, a feedback controller composed by a proportional and a derivative terms generates the control torques

$$\boldsymbol{\tau}_c = -\mathbf{K}(\mathbf{q} - \mathbf{q}^*) - \mathbf{D}\dot{\mathbf{q}} + g(\mathbf{q}). \quad (37)$$

Model-Based Quadratic Programming Control This control strategy is suited when adopting our learned second-order DS. In this case the control torques are generated as solution of the optimization problem

$$\begin{aligned} \min_{\ddot{\mathbf{q}}, \boldsymbol{\tau}, \boldsymbol{\xi}} \quad & \frac{1}{2} \ddot{\mathbf{q}}^T \mathbf{Q} \ddot{\mathbf{q}} + \boldsymbol{\tau}^T \mathbf{R} \boldsymbol{\tau} + \boldsymbol{\xi}^T \mathbf{W} \boldsymbol{\xi} \\ \text{s.t.} \quad & \mathbf{M}(\mathbf{q})\ddot{\mathbf{q}} = \mathbf{h}(\mathbf{q}, \dot{\mathbf{q}}) + \boldsymbol{\tau} + \boldsymbol{\xi} \\ & \mathbf{J}\ddot{\mathbf{q}} = \mathbf{f}(\mathbf{x}, \dot{\mathbf{x}}) + \boldsymbol{\xi} \\ & \mathbf{q}^- \leq \mathbf{q}_{t-1} + dt \dot{\mathbf{q}}_{t-1} + 1/2 dt^2 \ddot{\mathbf{q}} \leq \mathbf{q}^+ \\ & \dot{\mathbf{q}}^- \leq \dot{\mathbf{q}}_{t-1} + dt \ddot{\mathbf{q}} \leq \dot{\mathbf{q}}^+ \\ & \ddot{\mathbf{q}}^-, \boldsymbol{\tau}^- \leq \ddot{\mathbf{q}}, \boldsymbol{\tau} \leq \ddot{\mathbf{q}}^+, \boldsymbol{\tau}^+. \end{aligned} \quad (38)$$

In this case we impose track the desired acceleration generated by our second-order DS by imposing a relaxed inverse dynamics constraint in the quadratic optimization problem. The control torques are

$$\boldsymbol{\tau}_c = \boldsymbol{\tau}^*, \quad (39)$$

where $\boldsymbol{\tau}^*$ is extracted from the solution of the optimization problem in Equation (38).

[†]Code to reproduce simulation and real-robot results available at: <https://github.com/nash169/demo-learn-embedding>

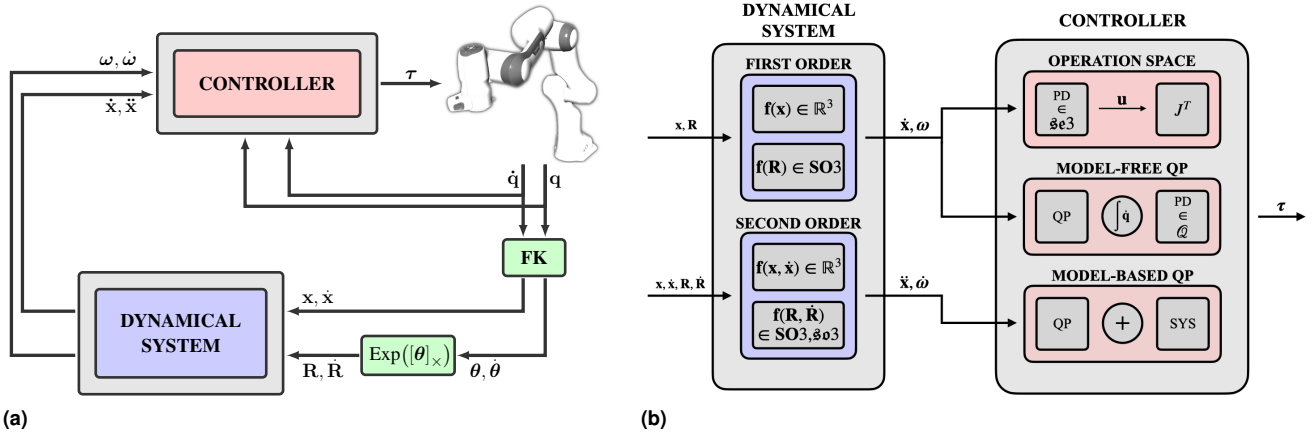


Figure 19. (a) Control Structure composed by high-level policy generate by the DS and a low-level controller producing torques; (b) depending on the DS deployed torques are generated via operation space control or model-free inverse kinematics QP for first-order DS and model-based inverse dynamics QP for second-order DS.

7.1 Trajectory Tracking Evaluation

In the case of first-order DS-based control, we deploy a standard proportional controller to generate an Euclidean space linear first-order DS that drives the end-effector to the starting point of each testing trajectory. Afterwards, we switch to the learned first-order DS.

When adopting second-order DS-based control, a critically damped proportional and derivative feedback is used to generate a standard Euclidean space linear second-order DS that drives the end-effector to the starting point of each testing trajectory. Afterwards, we switch to the learned second-order DS in order to perform the desired motion.

Table 3 reports the robotic experiment** results. Compared to model-based QP, Operation Space control and model-free QP yield worse performance in terms of DTWD but achieves much higher control frequency. The combination of model-based QP and second-order DS demonstrates the best DTWD. This comes at the cost of a reduced control frequency. Nevertheless the response time of such control makes it suitable for a large variety of high frequency applications.

Metric	1st Order DS		2n Order DS
	Operation Space	QP Inverse Kinematics	QP Inverse Dynamics
DTWD	2.26 ± 0.22	2.57 ± 0.1	2.17 ± 0.25
Frequency [Hz]	≈ 1300	≈ 1300	≈ 500

Table 3. Experimental results.

8 Conclusion

In this study, we presented an approach for learning non-linear DS grounded in a purely geometrical framework. Our approach involves defining a harmonic damped oscillator on a latent manifold. The inherent non-linearity of the DS is intrinsically captured by the curvature of this manifold so that the chart space representation of the DS’s vector field accurately replicates target trajectories. Our method ensures global asymptotic stability, which is maintained irrespective of the manifold’s curvature. Additionally, our method’s explicit embedded manifold’s representation grants direct control over the curvature of the space. This feature is

particularly advantageous in integrating the learning of non-linear DS with scenarios involving obstacle avoidance. Our approach is characterized by relatively minimal constraints. Specifically, the function approximator is required to learn a multi-scalar function from \mathbb{R}^d to \mathbb{R} , maintaining only C^1 -regularity. This constraint significantly reduces computational demands during both the training and query phases.

In conventional robotic motion generation, the process typically involves initially planning trajectories at a kinematic level, followed by the development of controllers for accurate trajectory tracking. Our approach aims at re-incorporating dynamics information within LfD framework by integrating two elements: (1) the utilization of high-level policies represented as more expressive second-order DSs, and (2) the application of model-based QP control for efficient one-step ID.

Limitations & Future Developments We demonstrated the application of learned DS. We believe that our approach can be adapted for joint space learning without violating joint limits. This involves initially learning a DS in high-dimensional joint space, followed by the application of local deformations to create energetic barriers, ensuring the robot remains within joint limits. In order to learn the embedding, we adopted a simple feed-forward network. Nevertheless, the use of controlled-smoothness kernels like the Matern kernel, coupled with probabilistic embedding, enhances noise robustness. Specifically, Gaussian Process Regression models can improve precision and query time, making our approach viable for online and adaptive learning. It is important to note that not every d -dimensional manifold can be isometrically embedded in a $d + 1$ dimensional Euclidean space. This limitation constrains the extent of non-linearity that can be effectively learned. A potential avenue for future research involves exploring embedding strategies for the manifold in a $d + n$ dimensional Euclidean

**beautiful-bullet simulator available at:

<https://github.com/nash169/beautiful-bullet>

franka-control control interface for Franka Research 3 available at:

<https://github.com/nash169/franka-control>

space. However, this approach would necessitate the use of n function approximators, potentially leading to a decrease in model interpretability. Currently, our methods cannot handle vector fields with limit-cycles or non-zero curl components. To address the first limitation, one could consider embedding compact Riemannian manifolds into higher-dimensional Euclidean spaces. For the second limitation, involving the manifold topology and the generation of non-zero curl vector fields, extending the theory to the embedding of pseudo-Riemannian manifolds into higher-dimensional Minkowski spaces may offer a solution.

Acknowledgements

Funding from the European Research Council (ERC) under the European Union's Horizon 2020 research and innovation program, Advanced Grant agreement No 741945, Skill Acquisition in Humans and Robots.

References

- Beik-Mohammadi H, Hauberg S, Arvanitidis G, Neumann G and Rozo L (2021) Learning Riemannian Manifolds for Geodesic Motion Skills. *arXiv:2106.04315 [cs]* .
- Bhardwaj M, Sundaralingam B, Mousavian A, Ratliff ND, Fox D, Ramos F and Boots B (2021) STORM: An Integrated Framework for Fast Joint-Space Model-Predictive Control for Reactive Manipulation. In: *Conference on Robot Learning*. pp. 750–759.
- Blocher C, Saveriano M and Lee D (2017) Learning stable dynamical systems using contraction theory. In: *2017 14th International Conference on Ubiquitous Robots and Ambient Intelligence (URAI)*. pp. 124–129.
- Bullo F and Lewis AD (2005) *Geometric Control of Mechanical Systems: Modeling, Analysis, and Design for Simple Mechanical Control Systems*. Texts in Applied Mathematics. Springer-Verlag.
- Bylard A, Bonalli R and Pavone M (2021) Composable Geometric Motion Policies using Multi-Task Pullback Bundle Dynamical Systems. In: *2021 IEEE International Conference on Robotics and Automation (ICRA)*. pp. 7464–7470.
- Cheng CA, Mukadam M, Issac J, Birchfield S, Fox D, Boots B and Ratliff N (2020) RMPflow: A Computational Graph for Automatic Motion Policy Generation. In: *Algorithmic Foundations of Robotics XIII*, Springer Proceedings in Advanced Robotics. Springer International Publishing, pp. 441–457.
- Dinh L, Sohl-Dickstein J and Bengio S (2016) Density estimation using Real NVP. *arXiv preprint arXiv:1605.08803* .
- do Carmo M (1992) *Riemannian Geometry*. Mathematics: Theory & Applications. Birkhäuser Basel.
- Fichera B and Billard A (2023) Hybrid Quadratic Programming - Pullback Bundle Dynamical Systems Control. In: *Robotics Research*, Springer Proceedings in Advanced Robotics. Springer Nature Switzerland, pp. 387–394.
- Figuroa N and Billard A (2018) A Physically-Consistent Bayesian Non-Parametric Mixture Model for Dynamical System Learning. In: *Conference on Robot Learning (CoRL)*. pp. 927–946.
- Huber L, Billard A and Slotine J (2019) Avoidance of Convex and Concave Obstacles With Convergence Ensured Through Contraction. *IEEE Robotics and Automation Letters* 4(2): 1462–1469.
- Joshi SC and Miller MI (2000) Landmark matching via large deformation diffeomorphisms. *IEEE transactions on image processing* 9(8): 1357–1370.
- Khansari-Zadeh SM and Billard A (2011) Learning Stable Nonlinear Dynamical Systems With Gaussian Mixture Models. *IEEE Transactions on Robotics* 27(5): 943–957.
- Khansari-Zadeh SM and Billard A (2012) A dynamical system approach to realtime obstacle avoidance. *Autonomous Robots* 32(4): 433–454.
- Kronander K and Billard A (2016) Passive Interaction Control With Dynamical Systems. *IEEE Robotics and Automation Letters* 1(1): 106–113.
- Lohmiller W and Slotine JJE (1998) On Contraction Analysis for Non-linear Systems. *Automatica* 34(6): 683–696.
- Mukadam M, Cheng CA, Fox D, Boots B and Ratliff N (2019) Riemannian Motion Policy Fusion through Learnable Lyapunov Function Reshaping. *arXiv:1910.02646 [cs, eess]* .
- Neumann K and Steil JJ (2015) Learning robot motions with stable dynamical systems under diffeomorphic transformations. *Robotics and Autonomous Systems* 70: 1–15.
- Perrin N and Schlehuber-Caissier P (2016) Fast diffeomorphic matching to learn globally asymptotically stable nonlinear dynamical systems. *Systems & Control Letters* 96: 51–59.
- Rahimi A and Recht B (2007) Random Features for Large-Scale Kernel Machines. In: *Advances in Neural Information Processing Systems*, volume 20. Curran Associates, Inc., pp. 0–1.
- Rana M, Li A, Ravichandar H, Mukadam M, Chernova S, Fox D, Boots B and Ratliff N (2019) Learning Reactive Motion Policies in Multiple Task Spaces from Human Demonstrations. In: *Conference on Robot Learning*. pp. 1457–1468.
- Rana MA, Li A, Fox D, Boots B, Ramos F and Ratliff N (2020) Euclideanizing Flows: Diffeomorphic Reduction for Learning Stable Dynamical Systems. In: *Learning for Dynamics and Control*. PMLR, pp. 630–639.
- Ratliff ND, Issac J, Kappler D, Birchfield S and Fox D (2018) Riemannian Motion Policies. *arXiv:1801.02854 [cs]* .
- Ratliff ND, Van Wyk K, Xie M, Li A and Rana MA (2021) Generalized Nonlinear and Finsler Geometry for Robotics. In: *2021 IEEE International Conference on Robotics and Automation (ICRA)*. pp. 10206–10212.
- Ravichandar H, Salehi I and Dani A (2017) Learning Partially Contracting Dynamical Systems from Demonstrations. In: *Conference on Robot Learning*. pp. 369–378.
- Simpson-Porco JW and Bullo F (2014) Contraction theory on Riemannian manifolds. *Systems & Control Letters* 65: 74–80.
- Sindhwani V, Tu S and Khansari M (2018) Learning Contracting Vector Fields For Stable Imitation Learning. *arXiv:1804.04878 [cs, stat]* .
- Solà J, Deray J and Atchuthan D (2021) A micro Lie theory for state estimation in robotics.
- Wensing PM and Slotine JJ (2020) Beyond convexity—contraction and global convergence of gradient descent. *Plos one* 15(8): e0236661.
- Williams G, Aldrich A and Theodorou EA (2017) Model Predictive Path Integral Control: From Theory to Parallel Computation. *Journal of Guidance, Control, and Dynamics* 40(2): 344–357.

Xie M, Van Wyk K, Li A, Rana MA, Wan Q, Fox D, Boots B and Ratliff N (2021) Geometric Fabrics for the Acceleration-based Design of Robotic Motion. *arXiv preprint arXiv:2010.14750*.

A Proofs of Prop. 1 & Thm. 1

In this appendix, we provide proofs for Prop. 1 and Thm. 1.

A.1 Proof of Prop. 1

A smooth embedding is an injective *immersion* $f : \mathcal{M} \rightarrow \mathcal{N}$ that is also a *topological embedding*. f , in order to be a topological embedding, has to yield a homeomorphism between \mathcal{M} and $f(\mathcal{M})$. Every map that is injective and continuous is an embedding in the topological sense.

Consider the local representative function in Eq. 6. Continuity follows directly from imposing $\psi \in C^r(\mathbb{R}^d)$ with $r \geq 1$. Also the injectivity property follows by the construction of the embedding. Let $\mathbf{x} \in \mathbb{R}^d$ and $\tilde{\mathbf{x}} \in \mathbb{R}^d$ two different points on \mathcal{M} , expressed in local coordinates, satisfying $\Psi(\mathbf{x}) = \Psi(\tilde{\mathbf{x}})$. Therefore

$$\begin{bmatrix} \mathbf{x} \\ \psi(\mathbf{x}) \end{bmatrix} = \begin{bmatrix} \tilde{\mathbf{x}} \\ \psi(\tilde{\mathbf{x}}) \end{bmatrix}. \quad (40)$$

In Eq. 40 the equality holds only if $\mathbf{x} = \tilde{\mathbf{x}}$.

$f : \mathcal{M} \rightarrow \mathcal{N}$ is an immersion if $f_* : T_p\mathcal{M} \rightarrow T_p\mathcal{N}$ is injective for every point $p \in \mathcal{M}$; equivalently $\text{rank}(f_*) = \dim(\mathcal{M})$. In order to analyze the rank of the pushforward map f_* we can look at its local coordinates components

$$f_{*j}^i = \partial_j (y \circ f \circ x^{-1})^i. \quad (41)$$

It is clear from Eq. 6 that for $i \leq \dim(\mathcal{M})$ we have $f_{*j}^i \equiv \delta_j^i$ where δ_j^i is the Kronecker symbol. Therefore $\text{rank}(f_*) = \dim(\mathcal{M}) = d$.

A.2 Proof of Thm. 1

Stability of the harmonic linearly damped oscillator in Eq. 2 can be proved via Lyapunov's second method for stability. Let $\gamma : I \rightarrow \mathcal{M}$ a curve on the manifold \mathcal{M} . We adopt the following energetic function in intrinsic notation

$$V(\gamma(t), v_{\gamma(t)}) = \frac{1}{2} g_{(\gamma(t))} (v_{\gamma(t)}, v_{\gamma(t)}) + \phi(\gamma(t)), \quad (42)$$

where $t \in I$ and $\gamma(t) \equiv p \in \mathcal{M}$. The time derivative, D_t , of V is given by

$$D_t V(p, v_p) = \nabla_{v_p} V(p, v_p) \quad (43)$$

$$= \frac{1}{2} \nabla_{v_p} (g_{(p)}(v_p, v_p)) + \nabla_{v_p} \phi(p). \quad (44)$$

For the compatibility of the Levi-Civita connection with the metric, $\nabla_{v_p} g = 0$, we can simplify Eq. 44 in

$$D_t V(p, v_p) = g_{(p)} (\nabla_{v_p} v_p, v_p) + \nabla_{v_p} \phi(p). \quad (45)$$

Eq. 45 can be expressed in local coordinates as

$$\begin{aligned} D_t V(p, v_p) &= g_{(p)} \left(-g^{ik} (\partial_i \phi + D_{ij} \dot{x}^j) \frac{\partial}{\partial x^k}, \dot{x}^i \frac{\partial}{\partial x^i} \right) \\ &\quad + \partial_i \phi \dot{x}^i \\ &= g_{(p)} \left(\frac{\partial}{\partial x^k}, \frac{\partial}{\partial x^i} \right) (-g^{ik} (\partial_i \phi + D_{ij} \dot{x}^j) \dot{x}^i) \\ &\quad + \partial_i \phi \dot{x}^i \\ &= -g_{ki} g^{ik} (\partial_i \phi + D_{ij} \dot{x}^j) \dot{x}^i + \partial_i \phi \dot{x}^i \end{aligned} \quad (46)$$

Given the symmetry of the metric tensor $g^{ik} = g^{ki}$ we have

$$\begin{aligned} D_t V(p, v_p) &= -\partial_i \phi \dot{x}^i - D_{ij} \dot{x}^j \dot{x}^i + \partial_i \phi \dot{x}^i \\ &= -D_{ij} \dot{x}^j \dot{x}^i \end{aligned} \quad (47)$$

We assumed $D \in \mathcal{S}_{++}^d$. Hence it follows $D \succ 0$ and $D_t V(p, v_p) < 0$.

B Kernel-Based Space Deformation

In this appendix we analyze kernel based deformation. In Sec. 5.1 we saw how this technique to effectively achieve obstacle avoidance.

B.1 Derivation of the Metric Tensor

The differential of the deformation function in the direction \mathbf{v} is given by

$$\begin{aligned} d\psi(\mathbf{x})[\mathbf{v}] &= \lim_{t \rightarrow 0} \frac{\exp - \frac{\|\mathbf{x} + t\mathbf{v} - \bar{\mathbf{x}}\|^2}{2\sigma^2} - \exp - \frac{\|\mathbf{x} - \bar{\mathbf{x}}\|^2}{2\sigma^2}}{t} \\ &= k(\mathbf{x}, \bar{\mathbf{x}}) \cdot \lim_{t \rightarrow 0} \frac{1}{t} (e^z - 1), \end{aligned} \quad (48)$$

where $z = -\frac{1}{\sigma^2} (t(\mathbf{x} - \bar{\mathbf{x}})^T \mathbf{v} + t^2 \mathbf{v}^T \mathbf{v})$. Dividing and multiplying Equation (48) by z and using the property $\lim_{z \rightarrow 0} \left(\frac{e^z - 1}{z} \right) = 1$ we have

$$\begin{aligned} d\psi(\mathbf{x})[\mathbf{v}] &= k(\mathbf{x}, \bar{\mathbf{x}}) \cdot \lim_{z \rightarrow 0} \left(\frac{e^z - 1}{z} \right) \cdot \lim_{t \rightarrow 0} \frac{z}{t} \\ &= k(\mathbf{x}, \bar{\mathbf{x}}) \cdot \lim_{t \rightarrow 0} -\frac{1}{\sigma^2} ((\mathbf{x} - \bar{\mathbf{x}})^T \mathbf{v} + t \mathbf{v}^T \mathbf{v}) \\ &= \left\langle -\frac{1}{\sigma^2} (\mathbf{x} - \bar{\mathbf{x}}) k(\mathbf{x}, \bar{\mathbf{x}}), \mathbf{v} \right\rangle = \langle \nabla \psi(\bar{\mathbf{x}}), \mathbf{v} \rangle. \end{aligned} \quad (49)$$

Via the pull-back of the embedding metric we recover the metric onto the manifold. In case of Euclidean (identity) metric for the ambient space we have

$$\mathbf{G}(\mathbf{x}) = \mathbf{I} + \frac{1}{\sigma^4} (\mathbf{x} - \bar{\mathbf{x}}) (\mathbf{x} - \bar{\mathbf{x}})^T k(\mathbf{x}, \bar{\mathbf{x}})^2. \quad (50)$$

The generic sum of kernels formulation is given by

$$\mathbf{G}(\mathbf{x}) = \mathbf{I} + \frac{1}{\sigma^4} \sum_{i=1}^N \alpha_i (\mathbf{x} - \bar{\mathbf{x}}_i) (\mathbf{x} - \bar{\mathbf{x}}_i)^T k(\mathbf{x}, \bar{\mathbf{x}}_i)^2. \quad (51)$$

MSE - 1e-3							
NEURONS PER LAYER							
		8	16	32	64	128	256
LAYERS	1	1.935 ± 2.144	0.839 ± 0.798	1.317 ± 0.652	0.632 ± 0.306	1.066 ± 0.528	0.543 ± 0.314
	2	0.209 ± 0.074	1.195 ± 2.370	0.133 ± 0.020	0.183 ± 0.083	0.159 ± 0.096	2.092 ± 2.073
	3	0.335 ± 0.325	0.192 ± 0.061	1.093 ± 1.990	0.193 ± 0.115	0.477 ± 0.480	3.507 ± 3.777
	4	0.232 ± 0.080	0.161 ± 0.077	0.121 ± 0.040	0.718 ± 1.282	2.094 ± 1.984	1.972 ± 2.235
	5	1.226 ± 2.111	0.844 ± 1.507	1.221 ± 2.296	0.702 ± 0.766	2.564 ± 1.451	2.598 ± 2.406
	6	0.686 ± 0.554	1.191 ± 2.356	2.318 ± 2.860	2.542 ± 2.516	3.887 ± 1.637	7.678 ± 4.950

Table 4. Ablation Study for the Neural Network function approximator.

B.2 Derivation of the Christoffel Symbols

Let $\tilde{\mathbf{x}} = \mathbf{x} - \bar{\mathbf{x}}$. The differential of the metric in the direction \mathbf{v} is given by

$$\begin{aligned}
d\mathbf{G}(\mathbf{x})[\mathbf{v}] &= \lim_{t \rightarrow 0} \frac{1}{t} \left(\mathbf{I} + \frac{1}{\sigma^4} (\tilde{\mathbf{x}} + t\mathbf{v})(\tilde{\mathbf{x}} + t\mathbf{v})^T k(\tilde{\mathbf{x}} + t\mathbf{v})^2 \right. \\
&\quad \left. - \mathbf{I} - \frac{1}{\sigma^4} \tilde{\mathbf{x}}\tilde{\mathbf{x}}^T k(\tilde{\mathbf{x}})^2 \right) \\
&= \frac{1}{\sigma^4} (\mathbf{v}\tilde{\mathbf{x}}^T + \tilde{\mathbf{x}}\mathbf{v}^T) k(\tilde{\mathbf{x}})^2 + \\
&\quad \underbrace{\lim_{t \rightarrow 0} \frac{1}{\sigma^4 t} (\tilde{\mathbf{x}}\tilde{\mathbf{x}}^T (k(\tilde{\mathbf{x}} + t\mathbf{v})^2 - k(\tilde{\mathbf{x}})^2))}_{\frac{\tilde{\mathbf{x}}\tilde{\mathbf{x}}^T}{\sigma^4} d\psi(\tilde{\mathbf{x}})^2[\mathbf{v}]} \\
&= \frac{1}{\sigma^4} (\mathbf{v}\tilde{\mathbf{x}}^T + \tilde{\mathbf{x}}\mathbf{v}^T) k(\tilde{\mathbf{x}})^2 \\
&\quad + \frac{1}{\sigma^8} \tilde{\mathbf{x}}\tilde{\mathbf{x}}^T (\mathbf{v}^T \tilde{\mathbf{x}}\tilde{\mathbf{x}}^T \mathbf{v}) k(\tilde{\mathbf{x}})^2. \tag{52}
\end{aligned}$$

Regrouping the terms in $1/\sigma^4$ and $k(\tilde{\mathbf{x}})^2$ we can express the differential of \mathbf{G} as

$$\begin{aligned}
d\mathbf{G}(\mathbf{x})[\mathbf{v}] &= \frac{1}{\sigma^4} ((\mathbf{v}\tilde{\mathbf{x}}^T + \tilde{\mathbf{x}}\mathbf{v}^T) k(\tilde{\mathbf{x}}) \\
&\quad + \frac{1}{\sigma^4} \tilde{\mathbf{x}}\tilde{\mathbf{x}}^T (\mathbf{v}^T \tilde{\mathbf{x}}\tilde{\mathbf{x}}^T \mathbf{v})) k(\tilde{\mathbf{x}})^2. \tag{53}
\end{aligned}$$

The Christoffel symbols of the first—without pre-multiplication for the metric inverse—multiplied by velocity can be derived by permuting the metric derivative as prescribed by Equation (10). This term is equivalent to what in mechanics is called Coriolis or apparent forces.

C Ablation Study

In order to select the correct model for the neural network used to learn the manifold embedding we performed an ablation study. In order to assess properly the model’s ability of learning the embedding, for the ablation study, we fixed the stiffness matrix to be spherical and we do not optimize for it. For the second-order DS, the damping matrix is set to be spherical and fixed as well, with diagonal values such that the systems exhibits critically damped behavior in flat space. In this case the non-linearity is achieved solely via the manifold’s curvature. For different number of layers and neurons within each layer we train each model till convergence. The training and testing dataset are given by 4 and 3 demonstrated trajectories, respectively. Each trajectory is composed by 1000 sampled points. Results are averaged over 10 runs of ADAM optimization on an NVIDIA RTX4090 24GB.

Tab. 4 reports the MSE results for different configurations. As it is possible to see from the results, a 2-layers configuration

with 32 neurons per layer is enough to achieve good performance with a high level of repeatability. By increasing the number of layers to 4, we observe an improvement of the performance. Nevertheless, we did not consider this marginal improvement sufficient to justify the additional overhead in terms of computational cost at training and query time. Therefore, for both the 2D and 3D experiments we opted for a neural network model composed by 2 hidden layers each of the composed by 32 neurons.